An Introduction to the Theory of Crystalline Elemental Solids and their Surfaces

Angelos Michaelides[1] and Matthias Scheffler[2]

[1]*London Centre for Nanotechnology and Department of Chemistry, University College London, London WC1E 6BT, UK*

[2]*Fritz-Haber-Institut der Max-Planck-Gesellschaft, Faradayweg 4-6, 14195 Berlin, Germany*

1. Introduction

The purpose of this chapter is to provide a basic and general introduction to the physical properties and electronic structures of elemental crystalline solids and their surfaces. Its main aim is to set the stage for what follows in the rest of this volume by providing an overview of our present understanding of the physics of solids and their surfaces, in general, and the underlying state-of-the-art theory, in particular.

Due to its very nature as an introductory text we shall, in most circumstances, refrain from going in to details, but hopefully present an up-to-date perspective (as of summer 2007). And, on the basis that one must understand elemental (i.e., one component) systems before one can understand compounds and other binary materials, elemental solids and surfaces will be considered only. On a similar basis the surfaces we discuss will mostly be flat, clean, and defect free. In addition, for reasons of space or because it is covered elsewhere in this volume many interesting aspects of solids and their surfaces will not be covered here. Specifically, vibrations or any other dynamic properties will not be considered; more often than not the electrons we discuss will be sitting happily in their ground state; magnetic and relativistic effects will largely be ignored; and our periodic table will exclude elements with unfilled shells of f electrons. Setting this list of exclusions aside, there remains, as we will see, still much to be said about the fundamental physical properties and electronic structures of elemental solids and their surfaces.

The chapter shall begin with a brief discussion of a few basic concepts of crystalline solids, such as an introduction to the common crystal types and a brief discussion of the cohesive properties of solids. Following this, the most widely used electronic structure technique for interrogating the properties of solids and their surfaces, namely density-functional theory will be introduced. We then discuss cohesion in bulk metals and semiconductors in more depth before reaching the main body of the chapter which involves a discussion of the atomic structures of crystalline solid surfaces, their energies, and their electronic structures in turn. We close with some general conclusions and perspectives for future work.

2. Some Basics

2.1 Crystalline solids are crystalline

The crystalline nature of materials such as salt or diamond is clearly apparent to the naked eye. It turns out, however, that crystals occur more often than expected in nature and many other materials which are not obviously crystalline in appearance possess a long range crystalline structure. Indeed metals, semiconductors, and many other insulators (aside from just diamond and salt) adopt crystalline structures.

The key property of crystalline solids is their inherent symmetry which arises because of the regular arrangement of their nuclei. It is interesting to note, however, that the actual definition of the term crystal provided by the International Union of Crystallography (IUC) is somewhat broader than a discussion based on periodicity of the atoms would imply. Specifically, IUC define a crystal as "any solid having an essentially discrete diffraction diagram". This definition, which is clearly somewhat ill-defined, has arisen mainly to account for the observations, from the 1980s, of quasiperiodic crystals, so-called "quasicrystals" [1]. Thus periodic crystals, which we will focus on here, are just a subset. How the nuclei are arranged leads to the crystal structure which is the unique arrangement of atoms in a crystal composed of a unit cell: a set of atoms arranged in a particular way which is periodically repeated in three dimensions on a lattice. The unit cell is given in terms of its lattice parameters, the length of the unit cell edges and the angles between them.

Crystallographers are adept at categorizing, counting, and systematizing crystal types according to their symmetry and crystal system. We will not venture into the world of crystallography except to say that for a general crystal structure in which objects of arbitrary symmetry are translated on a so-called Bravais lattice that there turn out to be 230 different symmetry groups that a lattice can have, known as the 230 space groups. When the object to be translated (the "basis") is completely symmetric, such as a single atom is, there turn out to be fourteen space groups (the fourteen Bravais lattices) falling into seven crystal structures (cubic, tetragonal, orthorombic, monoclinic, triclinic, trigonal, and hexagonal). Fortunately, for present purposes, we do not need to worry about all 230 space groups or even all fourteen Bravais lattices since elemental solids under standard conditions adopt a

very small number of structures. Indeed more than 70% [2] of all elemental solids adopt one of the following four crystal structures:

- Body-Centered Cubic (bcc): This is a simple cubic structure with atoms at the corner of a cube along with an additional atom at the center of the cube (Fig. 1(a)). The alkali metals and many early transition metals adopt this structure;
- Face-Centered Cubic (fcc): Again this is a simple cubic structure but now with an additional atom at the center of each square face (Fig. 1(b)). Most late transition and noble metals adopt this structure as well as the inert gas solids and some of the alkaline earth elements;
- Hexagonal Close Packed (hcp): This consists of two interpenetrating simple hexagonal lattices as shown in Fig. 1(c). Several transition metals adopt this structure;
- Diamond: This consists of two interpenetrating face-centered cubic lattices (Fig. 1(d)). The group IV elements (C, Si, Ge, and Sn) often crystalize in this structure.

All the elements we discuss in the following will be in one of these four crystal structures.

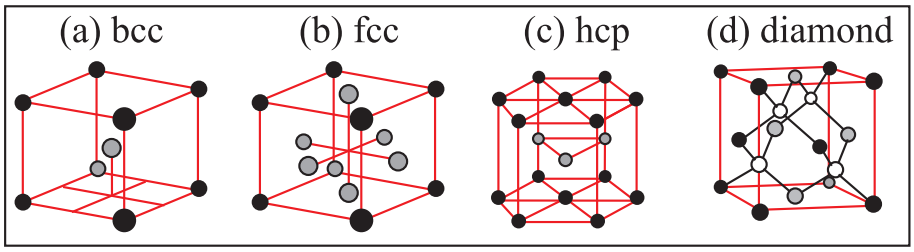

Figure 1: Illustration of the four types of crystal structure most commonly adopted by elemental solids. Certain atoms are shaded differently for clarity.

2.2 Cohesive energies

Another central property of solids is their *cohesive energy*, E^{coh}. This is the energy needed in order to rip a sample apart into a gas of widely separated atoms, as illustrated schematically in Fig. 2. If V denotes some structural parameter characteristic of a given

crystal, such as, for example, the unit cell volume, and V_o represents the value at the equilibrium crystal structure, we thus have

$$E^{\rm coh} \;=\; -\left(\frac{E(\{V_o\})}{M} - \frac{E(\{V\}\to\infty)}{M}\right). \qquad (1)$$

Here E is the energy of the solid, and M the number of atoms in the crystal. The energy that is used in (1) is the total energy (neglecting the zero point energy in this definition). The total energy is a large negative number, which leads to a positive $E^{\rm coh}$ in the definition above. Cohesive energies of elemental solids range from little more than a few meV per atom for the inert gases to just under 9 eV per atom for tungsten.

If one considers the variation of the energy with volume then, since both energy and volume are state functions, what we have is an equation of state (EOS) for the crystal. Equations of state for elemental solids are very often represented by a sketch like the one in Fig. 2. The difference between one material and the other is determined by variations in the depth, location, and curvature of the minimum. Many useful analytic expressions for the functional form of the EOS for solids have been developed. The most popular of them being the EOS due to Murnaghan [3], which is given by:

$$\frac{E(V)}{M} \;-\; \frac{E(V_o)}{M} \;=\; \frac{B_o V}{B_o'(B_o'-1)}\left[B_o'\left(1-\frac{V_o}{V}\right) \;+\; \left(\frac{V_o}{V}\right)^{B_o'} \;-\; 1\right] \quad , \qquad (2)$$

where the new quantities above are, B_o, the bulk modulus, and, B_o', its pressure derivative. The bulk modulus of a substance essentially measures its resistance to uniform compression and is defined as:

$$B_o = V\frac{\partial^2 E(V)}{\partial V^2}\bigg|_{V=V_o} \quad . \qquad (3)$$

We shall have more to say about cohesive energies and bulk moduli below.

2.3 The "types" of bonds in solids

It is useful to ask what "types" of bonds characterize solids in general and elemental solids in particular. In answering this question it is common to decompose the physical continuum of interactions that hold nature's many and varied solids together and conclude that there are five idealized types of bonding interaction, namely van der Waals, ionic, covalent, metallic, and hydrogen bonding. Let's now consider each briefly in turn:

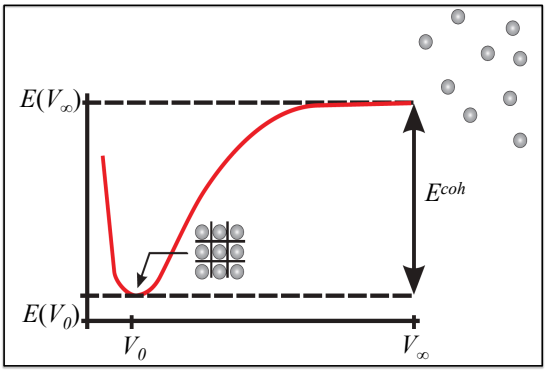

Figure 2: Schematic illustration of a typical energy-volume equation of state for a solid. The cohesive energy, E^{coh}, is indicated.

- Van der Waals Bonding: These are the weakest bonding interactions and arise through the instantaneous induced dipole-induced dipole (dispersive) forces between atoms [4]. The elements most commonly held together by van der Waals bonds are the rare gases Ne, Ar, Kr [5], and Xe [6]. These are the elements that have so-called filled valence shells. van der Waals forces also hold the layers of C in the graphite structure together and contribute to the binding in certain other solids (e.g. noble metals [7, 8]). The two overriding features of van der Waals forces are that they are: i) non-directional; and ii) weak (compared to the other types of bonding that we shall discuss). This leads in most cases to close-packed structures with cohesive energies that rarely exceed a few hundred meV per particle.

- Ionic Bonding: These are much stronger bonds than van der Waals bonds and arise through electrostatic attraction between oppositely charged ions. Typically this is realized in so-called ionic crystals such as the alkali halides in which an electropositive group I atom transfers an electron to an electronegative group VII atom resulting in two oppositely charged ions (in rather stable closed-shell configurations) which strongly attract each other. The resulting crystal structures that arise are those which offer optimal packing of differently sized ions.

- Covalent Bonding: Whilst ionic bonding is based on complete electron transfer between the atoms involved in a bond, covalent bonding is realized through the somewhat op-

posite scenario (still in our idealized pictures) in which electrons are equally shared between the bonding partners through the overlap of orbitals on adjacent atoms. Intrinsic to covalent bonding is therefore a strong *directionality* as opposed to the non-directional ionic or van der Waals bonds. As a result such materials do not necessarily adopt structures that arise from optimal packing. Instead the diamond and zincblende lattices are often favored.

- Metallic Bonding: The conceptual idea behind metallic bonding is that the valence electrons are highly delocalized; shared among the "community" of atoms in the solid and not localized on one particular atom or pair of atoms. In most abstract terms, such metals can thus be perceived as atomic nuclei immersed in a featureless electron glue. Thus metallic bonds are largely non-directional and close-packed structures are mostly adopted.

- Hydrogen Bonding: Generally hydrogen bonds occur when a covalently bound hydrogen atom forms a second bond to another element. Schematically the hydrogen bond is often represented as A-H...B. Invariably both A and B will be electronegative species (for example N, O, F, Cl). Compared to covalent or ionic bonds hydrogen bonds are weak with strengths ranging from about 100 meV to 500 meV. Generally it is believed that hydrogen bonds are mostly mediated by electrostatic forces; stabilized by the Coulomb interaction between the (partial) positive charge on hydrogen and the (partial) negative charge on the electronegative elements A and B. However, hydrogen bonds likely contain some covalent and van der Waals character too [9, 10].

No real solid can be classified 100% into any one of the above categories. Nonetheless, the division proves useful when seeking a qualitative understanding of the largely varying cohesive properties of materials. For *elemental* solids only three of these types of bonding interaction are found, namely metallic, covalent, and van der Waals. Since relatively little is known about the surfaces of pure van der Waals bonded solids, van der Waals bonding will not be discussed in the following. Instead we restrict our discussion on bonding in solids to metallic and covalent bonding. But, first we discuss density-functional theory.

3. The ABC of DFT

3.1 Theoretical Framework

Density-functional theory (DFT) is presently the most popular and robust theoretical approach available for solving the electronic structures of solids and their surfaces. Although far from a panacea for all physical problems in this domain (or any other) DFT has proven capable of computing a host of properties of condensed matter and their surfaces to reasonable accuracy. What "reasonable" accuracy is and what properties can be determined will be discussed. But before this we briefly introduce the theoretical framework that lies behind DFT, and the approximations that must be made to make it work in practice. We limit this introduction to the very basics of DFT since this is, after all, a surface physics book and several excellent and detailed texts on the subject exist [11, 12]. The reader already schooled in the basics of DFT may jump to section 4.

The Hamiltonian within the Born-Oppenheimer approximation is

$$H = T^e + V^{nuc-nuc} + V^{e-nuc} + V^{e-e} \quad . \tag{4}$$

T^e is the kinetic energy of each of the N electrons given by,

$$-\frac{1}{2}\sum_{i=1}^{N}\nabla_i^2 \quad , \tag{5}$$

where ∇_i^2 is the Laplacian operator acting on each of the i electrons. For simplicity and brevity in this section we use atomic units so that

$$e^2 = \hbar = m = 1 \quad , \tag{6}$$

where e is the electron charge, $\hbar$ is Planck's constant, and m is the electron mass. $V^{nuc-nuc}$ describes the electrostatic interaction between the M ions (or nuclei) with fixed coordinates $\boldsymbol{R}_{J,\ldots N}$ and charges $Z_{J\ldots N}$

$$\frac{1}{2}\sum_{I\neq J}^{M,M}\frac{Z_I Z_J}{|\mathbf{R}_I - \mathbf{R}_J|} \quad . \tag{7}$$

V^{e-nuc} is the electron-ion interaction energy,

$$-\sum_{i,I}^{N,M} \frac{Z_I}{|\mathbf{r}_i - \mathbf{R}_J|} \quad , \tag{8}$$

with electrons at positions r_i, and V^{e-e} is the electron-electron interaction energy given by,

$$\frac{1}{2}\sum_{i\neq j}^{N,N} \frac{1}{|\mathbf{r}_i - \mathbf{r}_j|} \quad . \tag{9}$$

The Hamiltonian can be written in one simple line as done above and slotted neatly into the Schrödinger equation,

$$H\Psi = (T^e + V^{nuc-nuc} + V^{e-nuc} + V^{e-e})\Psi = E\Psi \quad , \tag{10}$$

to deliver us the total energy of the system. The total energy of a given system at its ground-state, designated as E_0, is a highly sought after quantity. Many, if not most, physical properties of solids (or materials, in general) can be related to total energies or to differences in total energies.

However, solving the many-body Schrödinger equation is much easier said than done, and it is impossible to solve exactly for anything but the simplest model systems with 1, 2, or perhaps 3 electrons, or an infinite "jellium" system, the homogeneous electron gas (see section 4.1.2). Since solids contain lots ($\gg 10^{23}$) of electrons and the potential due to the nuclei is far from the constant of jelium we have a challenge. The root of the problem is well known. It is the quantity V^{e-e}, the electron-electron interaction, which contains all the many-body physics of the electronic structure problem. It depends on (at least) $3N$ spatial coordinates which are all coupled by the operator V^{e-e}.

There are many strategies for obtaining accurate approximate solutions to the many-body Schrödinger equation such as Green-function self-energy theory, quantum Monte Carlo, configuration interaction (CI), coupled cluster, and effective single-particle theories such as Hartree-Fock and DFT. The defining characteristic of DFT is that it aims to determine the ground state electron density distribution, n_0, of a system instead of the many-body wavefunction itself. Since real space is only 3 dimensional, regardless of the

number of electrons in the system, the required minimization is with respect to a function that depends only on 3 variables and not $3N$ variables [13]. In principle DFT is thus most useful for many electron systems. Indeed density-functional simulations of systems with thousands of electrons are now common and calculations with tends of thousands of electrons are not unheard of.

Approaches for tackling the many body problem based on the density have been around since the 1920s [14, 15]. The birth of modern DFT for the electronic structure problem, however, came with the realization and associated proof by Hohenberg and Kohn in 1964 [16] that the ground state electronic wavefunction, Ψ_0, is a unique functional of the ground state electron density, n_0, i.e.,

$$\Psi_0 = \Psi_0[n_0] \quad . \tag{11}$$

We don't reproduce the proof of this theorem here since the original paper is of unimprovable brevity and clarity. However, we do point the interested reader in the direction of ref. [17] for a subsequent more general formulation.

From the Hohenberg-Kohn theorem it follows that all observables are also functionals of the ground state density. The ground state density determines (unambiguously) the many-body Hamiltonian. And the latter, obviously, determines everything. In particular the ground state electronic energy, E_0^e, for a given configuration of the ions, is a functional, with a one to one correspondence, of n_0

$$E_0^e = E^e[n_0] = \min_{n(r)} \langle \Psi[n] | T^e + V^{e-nuc} + V^{e-e} | \Psi[n] \rangle \quad , \tag{12}$$

where the electron-nuclei interaction, which in this context is usually referred to as the "external potential", can be written explicitly in terms of the density as

$$V^{e-nuc}[n] = \int V(\mathbf{r}) n(\mathbf{r}) d^3\mathbf{r} \quad . \tag{13}$$

A variational principle, sometimes called the second Hohenberg-Kohn theorem, tells us that a successful minimization of the energy functional will yield the ground state density and

the ground state total energy [18].

A critical problem with eqn. (12), however, is the evaluation of the kinetic energy functional. Although in principle T^e is a function of the density an explicit closed expression does not exist. Thus a direct evaluation is not feasible, at least not without introducing significant errors. A practical method for obtaining $E^e[n]$ and thus minimizing the functional came from Kohn and Sham with the application of the Lagrangian method of undetermined multipliers [19]. Hereby, one uses the fact that the functional in eqn. (12) can be written as a fictitious density functional of a *non-interacting* reference system

$$E^e[n] = T_s^e[n] + \int V(\mathbf{r})n(\mathbf{r})d^3\mathbf{r} + E^{\text{Hartree}}[n] + E^{\text{xc}}[n] \tag{14}$$

where $T_s^e[n]$ is the kinetic energy functional of non-interacting electrons of density n. $E^{Hartree}$ is the Hartree energy describing the (classical) electron-electron Coulomb repulsion given by

$$E^{\text{Hartree}}[n] = \frac{1}{2}\iint \frac{n(\mathbf{r})n(\mathbf{r}')}{|\mathbf{r}-\mathbf{r}'|}d^3\mathbf{r}d^3\mathbf{r}' \quad . \tag{15}$$

And the final term, E^{xc}, is the exchange and correlation energy of DFT, into which all the complicated quantum-mechanical many-body effects are placed. The next step in this electronic structure problem is to define an effective potential,

$$\begin{aligned} V^{\text{eff}}(\mathbf{r}) &= \frac{\delta\left\{\int V(\mathbf{r})n(\mathbf{r})d^3\mathbf{r} + E^{\text{Hartree}}[n] + E^{\text{xc}}[n]\right\}}{\delta n(\mathbf{r})} \\ &= V(\mathbf{r}) + \int \frac{n(\mathbf{r}')}{|\mathbf{r}-\mathbf{r}'|}\,d^3\mathbf{r}' + \frac{\delta E^{\text{xc}}[n]}{\delta n(\mathbf{r})} \quad . \end{aligned} \tag{16}$$

From this one then obtains the single-particle Schrödinger equation:

$$\left\{-\frac{1}{2}\nabla^2 + V^{\text{eff}}(\mathbf{r})\right\}\varphi_{o_i}(\mathbf{r}) = \epsilon_{o_i}\varphi_{o_i}(\mathbf{r}) \quad , \tag{17}$$

which yields the orbitals that reproduce the density of the original many-body system

$$n(\mathbf{r}) = \sum_{i=1}^{N} |\varphi_{o_i}(\mathbf{r})|^2 \quad . \tag{18}$$

This is an *effective* single-particle equation, because V^{eff} depends on the solutions that we are seeking. The Hartree and exchange-correlation potentials depend on $n(\mathbf{r})$, which depends on the orbitals φ, which in turn depend on V^{eff}. Thus the problem of solving the Kohn-Sham equations (eqns. (16)-(18)) has to be done in a self-consistent (iterative) way. Usually one starts with an initial guess for $n(\mathbf{r})$, then calculates the corresponding V^{eff} and solves the Kohn-Sham equations for the φ. From these one calculates a new density and starts again. This procedure is then repeated until convergence is reached.

3.2 Approximations for Exchange and Correlation

So far, within the Born-Oppenheimer approximation, the theory is exact. However, we do not know the precise form of $E^{\text{xc}}[n]$ and $V^{\text{xc}}(\mathbf{r}) = \frac{\delta E^{\text{xc}}[n]}{\delta n(\mathbf{r})}$ into which we have placed all the complicated many-body physics. As the name suggests $E^{\text{xc}}[n]$ arises from a combination of two quantum mechanical effects: electron exchange and correlation. Briefly, electron exchange arises because a many-body wave function must by antisymmetric under exchange of any two electrons since electrons are fermions. This antisymmetry of the wave function, which is simply a general expression of the Pauli exclusion principle, reduces the Coulomb energy of the electronic system by increasing the spatial separation between electrons of like spin [20]. Likewise electron correlation further reduces the Coulomb energy between electrons of unlike spin because the motion of each individual electron is correlated with the motion of all others, helping also to keep electrons of unlike spin spatially separated. The sum of these two quantum mechanical effects as embodied in E^{xc} is incredibly difficult to describe. Indeed it is unclear if this functional can be given in a simple closed form at all. And so to get something useful out of DFT in practice one needs to approximate E^{xc}. There is no shortage of ways to do this, and as usual with a large number of anything, the anything gets categorized. Exchange and correlation functionals are no exception, being most often grouped in evolutionary terms (generations) or in biblical terms (the rungs of Jacob's ladder) [21]. Let's now look at some of the most popular types of exchange-correlation functional currently in use:

(a) *The local-density approximation (LDA)*: This is the simplest approximation, and can be written as

$$E^{\mathrm{xc-LDA}}[n] = \int n(r)\epsilon^{\mathrm{xc-LDA}}\left(n(\mathbf{r})\right)\, d^3\mathbf{r} \quad , \tag{19}$$

where $\epsilon^{\mathrm{xc-LDA}}$ is the exchange-correlation energy per particle of the homogeneous electron gas of density n, i.e., the exchange-correlation energy density is taken to be that of a uniform electron gas of the same density. The exchange energy is known exactly and the correlation energy is obtained by fitting to studies of Wigner, Gell-Man and Brueckner, and Ceperly and Alder [22–24]. Modern LDA functionals tend to be exceedingly similar, differing only in how their correlation contributions have been fitted to the many-body free electron gas data. The Perdew-Zunger (PZ) [25], Perdew-Wang (PW) [26] and Vosko-Wilk-Nusair (VWN) [27] functionals are all common LDA functionals [28].

Strictly, the LDA is valid only for slowly varying densities. Experience with calculations of atoms, molecules, and solids shows that eq. (19), *i.e.*, the LDA works surprisingly well, and much current understanding of surfaces comes from LDA calculations. A partial rationalization of the success of LDA is provided by the observation that it satisfies a number of so-called sum rules [29–32].

(b) *The generalised gradient approximation (GGA)*: These are the second generation functionals (sitting on the second rung of Jacob's ladder) in which the gradient of the density, $\nabla n(\mathbf{r})$, at each coordinate is taken into account as well as the density itself:

$$E^{\mathrm{xc-GGA}}[n] = \int n\epsilon^{\mathrm{xc-LDA}}\left(n(\mathbf{r})\right)\nabla n(\mathbf{r})\, d^3\mathbf{r} \quad . \tag{20}$$

Thus GGAs are "semi-local" functionals, comprising corrections to the LDA while (again) ensuring consistency with known sum rules. For many properties, for example geometries and ground state energies of molecules, GGAs can yield better results than the LDAs. Although, as we will see, for the properties of metals and their surfaces, GGA results are not necessarily superior to LDA results. The most widely used GGAs in surface physics are the PW91 [26] functional, and its close relative PBE [33]. PBE by now has several off-spring [34], revPBE [35], RPBE [36], PBE-WC [37], MPBE [38], RPBEsol [39], optPBE [40], etc, etc... Some of the off-spring (by restoring the density-gradient expansion for exchange) as well as AM05 [41] offer improved performance for some solids and surfaces,

as we briefly discuss below.

(c) *The meta-GGAs*: These are the third generation functionals (third rung of Jacob's ladder) and use the second derivative of the density, $\nabla^2 n(\mathbf{r})$, and/or kinetic energy densities, $\tau_\sigma(n) = 1/2\Sigma_i|\nabla\varphi_i(n)|^2$, as additional degrees of freedom. In gas phase studies of molecular properties and solids meta-GGAs such as TPSS [42] and, in particular, revised TPSS [43] have been shown to offer improved performance over LDAs and GGAs.

(d) *The hybrid functionals*: These fourth generation functionals add "exact exchange" calculated from Hartree-Fock (HF) theory to some conventional treatment of DFT exchange and correlation [44]. The most widely used, particularly in the quantum chemistry community, is the B3LYP [45] functional which employs three parameters, a_{1-3} (determined through fitting to experiment [21]) to control the mixing of the HF exchange and density functional exchange and correlation. It takes the following form:

$$E^{xc} = E^{xc-LDA} + a_1(E^{x-HF} - E^{x-LDA}) + a_2\Delta E^{x-GGA} + a_3\Delta E^{c-GGA} \quad . \tag{21}$$

Reformulating this to eliminate two parameters leads to an equation of the form

$$E^{xc} = E^{xc-GGA} + a(E^{x-HF} - E^{x-GGA}) \quad , \tag{22}$$

and setting $a = 1/4$ (at one stage justified on the grounds of perturbation theory) leads to a class of functionals with only as many parameters as their underlying GGAs. If PBE is the GGA used in eqn. (22) we arrive at the hybrid PBE0 functional [46]. Such functionals have been shown to offer noticeably improved performance over LDA and GGA functionals for the calculation of gas phase properties of molecules and band gaps in solids. Applications of hybrid functionals and screened hybrid functionals [47] to solids have gradually begun to appear over the last few years [48], although not-unexpected problems with metals have been identified and discussed (e.g. [49–53]).

(e) The last few years have seen some very exciting developments on yet higher rungs of the ladder of exchange-correlation functionals. In particular approaches which explicitly account for correlation have emerged such as the random phase approximation (RPA)

within the adiabatic connection fluctuation dissipation theorem. Very recently RPA has been applied to solids and surfaces with some very encouraging results (e.g. [54–58]).

3.3 Other Approximations and Practicalities of Condensed Phase DFT calculations

Before we can take our electronic structure theory with our chosen exchange-correlation functional off to compute a solid or a surface there are several other issues to deal with and approximations to make. Good reviews exist on what it takes to perform a reliable condensed matter DFT simulation (see for example, refs. [59–61]), so we don't go into the details here, instead merely point out some of the relevant issues necessary to appreciate the discussion that comes later.

(a) *Periodicity and simulation cells:* A finite chunk of crystal contains many atoms; 10^{23} is not a large number when discussing the number of atoms in a crystal. Fortunately, crystalline solids have, by definition, periodicity. This periodicity introduces important elements of simplicity. Notably Bloch's theorem can be applied, allowing the electronic structure problem for infinite solids to be tackled in periodic 3D simulation cells, primitive or otherwise. Surfaces, although only periodic in two dimensions, can nonetheless be computed within periodic 3D simulation cells by introducing a vacuum region into the unit cell. In particular the introduction of a vacuum region along just one dimension, for example along the z axis in Fig. 3, partitions the unit cell into regions of solid (slab) and vacuum. The periodic boundary conditions ensure that the slab is infinite in the x and y directions, and also along the z direction the slab and vacuum stack extends infinitely. It is common to use this periodic slab model in simulations of solid surfaces and results from such slab model simulations will be discussed frequently throughout this chapter [62].

(b) *Basis sets and electron-ion interactions:* The primary computational task in a DFT calculation is the solution of the Kohn-Sham equations for a given atomic structure and chemical composition. Invariably for a condensed phase system this requires the use of a set of basis functions with which to expand the Kohn-Sham orbitals φ. This choice of basis set is of critical importance to the accuracy of an electronic structure calculation; so much

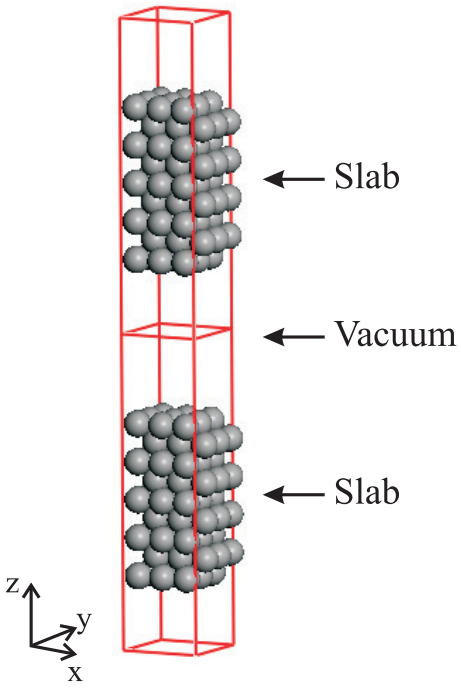

Figure 3: Illustration of the supercell approach to model surfaces: the surface is represented by a periodic stack of slabs separated by vacuum.

so that first-principles methods are often named according to the basis functions they employ.

Basis sets are constructed from either atom-centered functions or from non-atom-centered functions or a combination of both. For condensed phase simulations non-atom-centered basis sets such as plane waves are currently the most popular scheme. Often the choice of basis set goes hand in hand with the choice of electron-ion interaction and indeed if one chooses to use purely a plane-wave basis set one must replace the full and deep electron-ion potential of nuclei plus core electrons with some approximate potential that can be described with a tractable number of plane waves. Hiding the core electrons in, for example, a pseudopotential (PP) or something similar like a projector augmented wave (PAW) potential are two possibilities [61, 63, 64]. And, indeed, the plane-wave plus PP or PAW recipe is currently the most popular one for electronic structure simulations of solids and their surfaces [61, 65]. Alternatively, one may choose to use a mixed basis set in which the computational cell is partitioned in to distinct regions, each of which is described with different functional forms for the basis. One particular scheme we mention here is the

full-potential linearized augmented plane-wave (FP-LAPW) method [66]. In this scheme plane waves are used to describe a predefined interstitial region between the atoms in the solid and the regions close to the cores of the atoms, within predefined "muffin-tin" spheres, are described by radial functions and spherical harmonics. The FP-LAPW approach is more computationally expensive than the plane-wave plus PP or PAW approach, but has the advantage of being a truly all-electron approach. In many cases in solid state systems FP-LAPW calculations thus provide the benchmark "gold standard" theoretical data with which to compare other methods. Where possible in the following we will thus discuss results from FP-LAPW calculations. However, it is worth noting that in the last few years accurate full potential all-electron calculations for solids using numeric atom-centred orbitals have seen a rise in popularity [67, 68].

4. Bonding in Solids

We now introduce some simple models for bonding in metals and semiconductors such as jellium and hydridization and at the same time assess our theoretical tool of choice, DFT, at predicting some of the central cohesive properties of solids.

4.1.1 Bonding in Metals

The essential characteristic of metallic bonding is that the valence electrons are delocalized among a lattice of metal atoms. Delocalization is the consequence of heavy overlap between the individual valence wavefunctions resulting in the valence electrons being shared by all the atoms in the "community". In most abstract terms, metals can thus be perceived as atomic nuclei immersed in a featureless sea (or "glue") of electrons. This electron sea leads to bonding that is generally not directional, resulting in close-packed crystal structures being often favored, such as the fcc and hcp structures. Because of the strong overlap of the orbitals the resultant electronic wavefunctions or bands of a metal will thus exhibit a strong dispersion in reciprocal space, $\boldsymbol{k}$ space. As an example we show in Fig. 4(a) the band structure of bulk Cu.

A useful quantity for interpreting the characteristics of chemical bonding, that we will

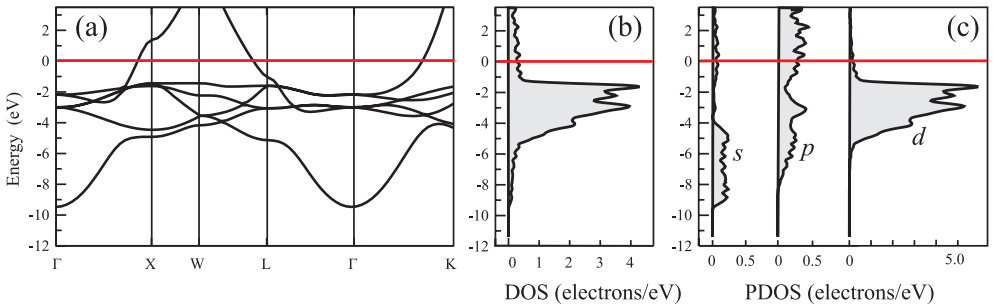

Figure 4: Band structure (a), density of states (DOS) (b), and partial DOS (PDOS) (c) for bulk Cu as computed from a plane-wave pseudopotential DFT calculation within the LDA. In (c) the PDOS are projected onto Cu s, p, and d orbitals. The energy zero is the Fermi level (computed by the authors).

use throughout to examine metals, is the density of states. It is defined as

$$N(\epsilon) = \int n(\mathbf{r}, \epsilon) d\mathbf{r} = \sum_{i=1}^{\infty} \delta(\epsilon - \epsilon_i) \quad , \tag{23}$$

where the sum goes over all eigenstates (orbitals) with eigenvalues, ϵ_i, of the Kohn-Sham Hamiltonian. Cutting through this DOS is the Fermi level (E_F): the energy below which the one-electron levels are occupied and above which they are not, in the ground-state of a metal. Again we illustrate these concepts with the example of Cu, displayed in Fig. 4(b). For future reference, we note that for metals the Fermi level is equivalent to the chemical potential of the electrons at 0 K.

Another useful quantity, which is not readily accessible in any simple manner from experiment, is the state-resolved DOS, also called the projected DOS (PDOS):

$$N_\alpha(\epsilon) = \sum_{i=1}^{\infty} |\langle \phi_\alpha | \varphi_i \rangle|^2 \delta(\epsilon - \epsilon_i) \quad , \tag{24}$$

where ϕ_α is a properly chosen localized function whose overlap with the Kohn-Sham orbitals is determined. Often it proves useful to pick individual atomic orbitals or groups of atomic orbitals as localization functions upon which to project the electron density. For example, we have done this for Cu in Fig. 4(c) from where it can be seen that the Cu valence band is comprised of s, p, and d states.

4.1.2 Simple Metals and Jellium

It turns out that for the s and p block metals a simple model, namely the *jellium model* provides useful insight. In this model the discrete nature of the ionic lattice is replaced with a smeared out uniform positive background exactly equal to that of the valence electron gas. In jellium, each element is completely specified by just the electron density $n = N/V$, where N is the number of electrons in the crystal and V is its volume. Often the electron density is given in terms of the so-called Wigner-Seitz radius, r_s, where $r_s = (3/4\pi n)^{1/3}$ which corresponds to the spherical volume in Bohr atomic units available to one valence electron. The r_s of real metals range from ~ 2 (high density) to ~ 6 (low density).

For the completely smeared out constant ion density of jellium, the electron-ion (E^{e-nuc}) and ion-ion ($E^{nuc-nuc}$) energies cancel exactly with the Hartree energy ($E^{Hartree}$), *i.e.*, $E^{e-nuc} + E^{nuc-nuc} + E^{Hartree} = 0$. This then leaves

$$E/N = T_s + E^{xc} \quad , \tag{25}$$

where, à la DFT, T_s is the kinetic energy of the non-interacting electron gas and E^{xc} is the exchange and correlation energy. It is easy to show that the kinetic energy of the free electron gas is, in atomic units, $T_s = \frac{2.21}{r_s^2}$ [2, 69]. The exchange energy per particle can also be computed exactly from HF theory and together with accurate parameterizations of the correlation energy, the binding energy of jellium (in atomic units) is

$$E/N = \underbrace{\frac{2.21}{r_s^2}}_{T_s} \; \underbrace{- \; \frac{0.916}{r_s} \; - \; 0.115 \; + \; 0.0313 \ln r_s}_{E^{xc}} \quad . \tag{26}$$

The kinetic energy contribution to eqn. (26) is, of course, positive and repulsive, whereas the contribution from electron exchange and correlation is attractive. The latter is the glue that holds metals together and arises from the formation of the so-called exchange-correlation hole. This is a region of charge depletion around each electron due to the fact that electrons of like spin keep apart primarily because of the antisymmetry

condition and the motion of electrons of like and unlike spin is correlated due to the Coulomb repulsion between electrons (section 3.2). The main consequence of this region of charge depletion around each electron for the present discussion is that each electron feels an attractive potential from the surrounding positive jellium background. Therefore the equilibrium bound state of minimum total energy results from a balance between the kinetic energy of the valence electrons, which tries to push the atoms apart, and the exchange-correlation energy, which tries to pull them together. The minimum in this binding energy curve for jellium occurs at an $r_s = 4.2$ with a binding energy of 2.2 eV/atom. This is quite close to the cohesive energy, E^{coh}, of real *sp* metals which fall at around 1-2 eV/atom [70] and quite good agreement considering the simplicity of the model. Indeed jellium can be modified [2, 71–73] to do better and to describe a range of properties (for example, phonon spectra, optical absorption, superconducting transition temperatures, and equations of states) by replacing our initial approximation of a uniform positive background with something less extreme, like, for example, a weak pseudopotential.

4.1.3 Transition Metals and Tight-Binding

The transition metals belong to three series in the periodic table which correspond to the progressive filling of $3d$, $4d$, and $5d$ states. The presence of the d electrons changes the picture of bonding in these metals considerably from the simple metals and the jellium description of metallic bonding no longer suffices. Notably the cohesive energies rise to significantly more than the 1-2 eV/atom of the simple metals and follow a roughly parabolic variation across the transition metal series. For example, E^{coh} goes from 4.36 to 6.66 to 3.92 eV/atom from Y to Ru to Pd [74].

To understand this variation in E^{coh} it is useful to recognize that the electronic structure of the transition metals is comprised of two largely separate contributions: a broad free-electron-like *sp* band; and a considerably narrower d band. We saw this already with the PDOS plot of Cu (Fig. 4) and we illustrate it again schematically in the top part of Fig. 5(a). The d band is narrower than the *sp* band simply because the d valence orbitals are more localized and thus the overlap between them is more directional and shorter ranged. For example, the peak maximum of the $3d$ radial distribution for the $3d$ transition metals is

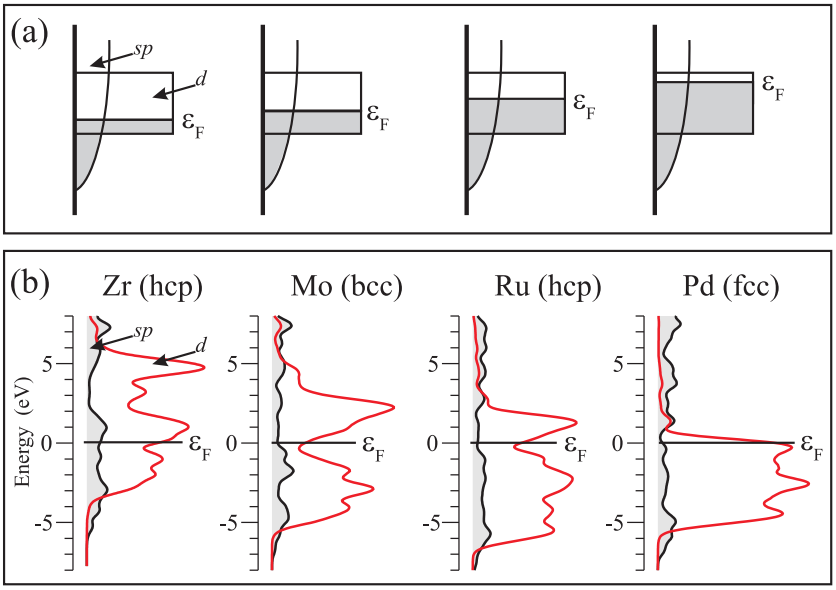

Figure 5: (a) Schematic illustration of the relative filling of the d and sp densities of states as one moves from left to right across the transition metals. (b) Computed d and sp partial densities of states for several $4d$ transition metals, as obtained from a plane-wave pseudopotential DFT calculation within the LDA (computed by the authors).

typically >2 times closer to the core than the peak maximum of the $4s$ radial distributions [75]. This is a consequence of the fact that the $3d$ orbitals do not have lower energy d states, but the $4s$ orbitals need to be orthogonal to the 1,2, and $3s$ states. For such systems where there is small overlap between orbitals a tight-binding description in which the system is described by a simple linear combination of atom centered d orbitals can be used. The simplest version of this applied to the transition metals is the so called *rectangular d band model* of Friedel, where the d PDOS is assumed to be rectangular and $E^{\rm coh}$ takes the following form

$$E^{\rm coh} \propto \frac{W}{20} N_d(N_d - 10) \quad , \tag{27}$$

where W is the width of the d band and N_d is the number of d electrons. As one can see from eqn. (27) this model leads to a parabolic shape for the cohesive energy over the transition metal series and suffices at catching the basic chemical behavior that as one moves from left to right across the transition series one gradually fills up the d band, which, of course, involves filling the bonding, non-bonding and then anti-bonding

states until finally at the end of the transition metal series, the d band is completely filled. We illustrate this progression schematically in Fig. 5(a). This crude model captures the qualitative cohesive trend over a large number of elements and with a suitable choice of the parameter W and the introduction of an (empirical) proportionality constant to account for repulsion between the ions in the solid, also the absolute cohesive energies come out quite well. For the interested reader a detailed discussion on this topic can be found in the book by Desjonquères and Spanjaard [76].

We will see when we move to surfaces that the rectangular d band model helps to explain trends in surface electronic structures also. However, it must be recognized that this is merely a highly simplified model of the electronic structures of transition metals. In reality the DOS results from an integration over the Brillouin zone and so points that occur often and where the bands are relatively flat will give rise to a high density of states. This implies that the detailed shape of the d DOS is more complex than the simple rectangular model assumes and reflects the lattice type of the crystal rather than the filling. This can be seen in Fig. 5(b) where PDOS from self-consistent DFT calculations are shown for four $4d$ metals (Zr, Mo, Ru, and Pd). The d PDOS of the fcc metal Pd is rather similar to the d PDOS of Cu (also fcc) (Fig. 4). The two hcp metals Zr and Ru exhibit similar d PDOS and the bcc metal metal Mo, exhibits a large dip in the center of the d PDOS characteristic of bcc metals [77]. Indeed these "canonical" shapes of the DOS of hcp, bcc, and fcc structures explains the trend through the periodic table, e.g. from Y to Ag. Despite the added complexity of the DOS, however, it can be seen from Fig. 5 that the trend embodied in the rectangular d band model with regard to d band filling holds, which is, of course, the reason for the qualitative success of the model.

4.1.4 DFT for the Cohesive Properties of Metals?

Simple models aside, if we choose to perform a self-consistent DFT calculation in which we explicitly treat the ionic lattice with, for example a pseudopotential or full potential treatment, what level of accuracy can we expect to achieve? As always the answer depends on the properties we are interested in and the exchange-correlation functional we use. DFT has been used to compute a whole host of properties of metals, such as phonon

dispersion curves, electronic band structures, solid-solid and solid-liquid phase transitions, defect formation energies, magnetism, super-conducting transition temperatures, and so on. However, to enable a comparison between a wide range of exchange-correlation functionals, we restrict ourselves here to a discussion of only three key quantities, namely (i) $E^{\rm coh}$; (ii) a_0, the equilibrium lattice constant; and (iii) B_0, the bulk modulus.

Table 1 lists a number of DFT and experimental values for a simple metal Al, two noble metals Cu and Ag, and a transition metal with an unfilled d shell Pd. One example from each of the first four generations of exchange-correlation functional is given so as to provide a flavor of the current state of DFT for the cohesive properties of metals. In addition to the LDA we show results from the PBE (GGA), TPSS (meta-GGA), and PBE0 (hybrid) functionals. Let's consider each functional in turn and see what general conclusions can be drawn:

(a) LDA predicts the smallest lattice constants, the largest bulk moduli, and the largest cohesive energies. Moreover, compared to experiment the LDA lattice constants are smaller (~ -2 %), the bulk moduli are larger ($\sim +10$ %), and the cohesive energies are larger ($\sim +20$ %) for these four materials. These quantities are naturally all related and reflect the now well-established fact that LDA generally overbinds metals (and other solids and molecules). See ref. [80].

(b) The PBE (GGA) functional results are generally closer to experiment than LDA. The average errors for these metals are +1.3 % for the lattice constants, and -5 % for both the bulk moduli and cohesive energies. Naturally this improvement leads to larger lattice constants, smaller bulk moduli, and smaller cohesive energies. Indeed it is now clear that performance is very sensitive to the solids considered [80].

(c) The TPSS (meta-GGA) functional is somewhat difficult to assess. For lattice constants it is significantly better than LDA and GGA with an error of only 0.5 %, getting all four metals within 0.04 Å. For the bulk moduli, however, it is not as accurate with an error of 11 %, and we for $E^{\rm coh}$ we are not aware of any reported values. There is now a revised-TPSS functional which for many properties improves over the original TPSS

Table I: Bulk properties of Al, Cu, Pd, and Ag, as computed from DFT with the LDA, PBE, TPSS, and PBE0 exchange-correlation functionals. All data is taken from Refs. [78], [48], and [79]. Ref. [78] is an all-electron study with a Gaussian basis set. Data from ref. [48] has been obtained with the plane-wave plus PAW method and data from ref. [79] has been obtained with the FP-LAPW method. The experimental values in parenthesis have been corrected for zero point effects.

		a_0(Å)			B_0 (Mbar)			E^{coh}(eV)		
		Ref. [78]	Ref. [48]	Ref. [79]	Ref. [78]	Ref. [48]	Ref. [79]	Ref. [78]	Ref. [48]	Ref. [79]
Al	LDA	4.01		3.98	0.82		0.84			4.07
	PBE	4.06	4.04	4.04	0.76	0.77	0.78		3.43	3.60
	TPSS	4.04			0.85					
	PBE0		4.01			0.86			3.39	
	expt.		4.03 (4.02)			0.79			3.39	
Cu	LDA	3.53		3.52	1.88		1.92			4.57
	PBE	3.64	3.64	3.63	1.50	1.36	1.42		3.48	3.51
	TPSS	3.59			1.71					
	PBE0		3.64			1.30			3.05	
	expt.		3.60 (3.60)			1.42			3.49	
Pd	LDA	3.85		3.85	2.35		2.22			5.04
	PBE	3.95	3.94	3.95	1.77	1.66	1.63		3.71	3.63
	TPSS	3.92			2.00					
	PBE0		3.92			1.72			2.88	
	expt.		3.88 (3.88)			1.95			3.89	
Ag	LDA	4.00			1.49					
	PBE	4.13	4.15		1.06	0.89			2.52	
	TPSS	4.08			1.27					
	PBE0		4.14			0.87			2.33	
	expt.		4.07 (4.06)			1.09			2.95	

functional [43].

(d) The hybrid PBE0 functional does not appear to offer any clear improvement over the other functionals. At an error of 1 % for the lattice constants PBE0 performs worse than TPSS and is similar to PBE. Furthermore, errors for the bulk moduli and cohesive energies, both of 10 % are rather disappointing; offering worse performance than the regular GGA-PBE [81]. Since using functionals with exact exchange when treating solids (or more precisely periodic systems) generally leads to a considerable increase in computational effort (about a factor of 35 with a plane-wave basis set according to one estimate [82]) it is difficult to justify their use if one is purely interested in determining properties such as the lattice constant, bulk modulus, and cohesive energy of metals. In addition other hybrid functionals, such as B3LYP, can perform even worse [83], with, for example, the computed E^{coh} of Mg differing from experiment by almost 100 % [53].

In conclusion, of the few functionals discussed here, no single one stands out as being significantly superior to the others for treating metals. All of them perform reasonably well in capturing the large variation in lattice constants and bulk moduli. Periodic trends in E^{coh} are also reproduced. As for the quantitative determination of E^{coh}, however, the situation is far from satisfactory with the choice of exchange-correlation functional crucial to the value obtained. Moreover, there is no convincing proof to tell us that, for example, GGA will always be superior to LDA. We note, however, that since about 2007 some excellent progress in state-of-the-art electronic structure methodologies for solids has been made with the development of exchange-correlation functionals together with RPA for correlation. The interested reader is referred to refs. [43, 54–57, 80, 84–86] for accounts of how these various approaches perform. Notwithstanding this recent progress, the identification of a functional, or, indeed any electronic structure method that is computationally efficient and consistently able to calculate E^{coh} for metals (and other solids) with an accuracy of, for example, less than 5 % error remains an important unresolved issue in materials science.

4.2.1 Semiconductors and Covalent Bonding

The metallic bonding described in the last section is based largely on a delocalization of

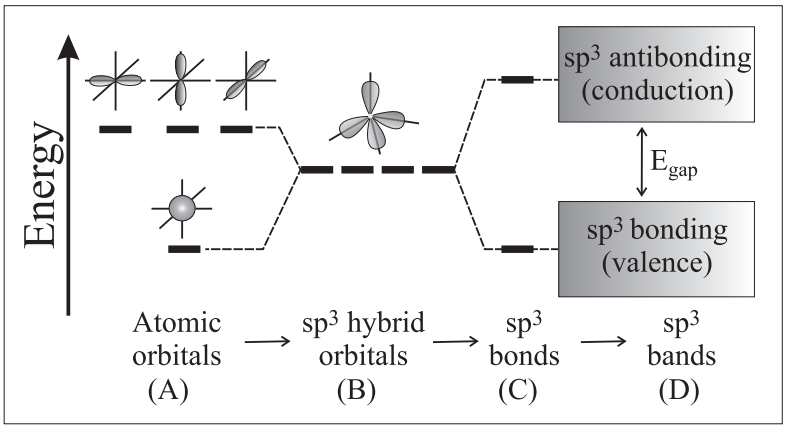

Figure 6: Illustration of the formation of sp^3 valence and conduction bands in the tetrahedral semiconductors. As one goes from C to Si to Ge to Sn the size of the atoms increase, which increases the band widths and decreases the band gap ($E_{\rm gap}$).

electrons throughout the entire lattice, yielding, as we have said, a sea of electrons or structureless glue. In covalent bonding, on the other hand, electrons are shared between adjacent bonding partners through the strong overlap of the wavefunctions on the adjacent atoms. The extent of this overlap depends in part on the orbital character of the wavefunctions involved, i.e., in which directions the bonding partners lie. Intrinsic to covalent bonding is therefore a strong directionality as opposed to the largely non-directional metallic bonds. When directionality matters the preferred crystal structures will not simply result from an optimum packing of spheres but instead result from optimal orbital overlap and bonding between the partners. Often this leads covalent solids to adopt tetrahedral structures such as the diamond and zincblende structures; with the classic examples of such solids being the tetrahedral group IV elements (C, Si, Ge, and α-Sn). A useful concept for understanding such structures and indeed covalent materials in general is what is known as *hybridization*, which we now briefly discuss.

Hybridization or hybrid orbital formation has proved to be an extremely helpful and instructive concept for understanding the structure and bonding in many covalent materials (solids and molecules). Here we introduce the basic ideas of hybrid orbital formation with the single illustrative example of the group IV elements, C, Si, Ge, and Sn. All four elements have four valence orbitals with the valence configuration ns^2, np^2 (A in Fig. 6). One finds

that it is possible to make linear combinations of these four valence orbitals to yield a new set of hybrid orbitals. The particular set of hybrid orbitals relevant to the present discussion are the sp^3-*hybrid functions*. These four sp^3 hybrid orbitals are linear combinations of the original orbitals and can be written down as

$$\phi^1 = \frac{1}{2}(s + p_x + p_y + p_z) \tag{28}$$

$$\phi^2 = \frac{1}{2}(s + p_x - p_y - p_z) \tag{29}$$

$$\phi^3 = \frac{1}{2}(s - p_x + p_y - p_z) \tag{30}$$

$$\phi^4 = \frac{1}{2}(s - p_x - p_y + p_z) \tag{31}$$

yielding orbitals that point to the four corners of a tetrahedron (B in Fig. 6). This set of hybrid orbitals corresponds to an excited state of the atom, i.e., this set of hybrid orbitals is less stable than the original set of atomic orbitals, by an amount known as the hybridization energy. In certain circumstances, however, it is possible for hybrid orbitals on adjacent atoms to bond more effectively with each other than the atomic orbitals would have done and in so-doing render the composite (molecule, solid) system more stable. Or, in other words, the energy gain upon chemical bonding between the hybrid orbitals outweighs the hybridization energy cost. For the present example of sp^3 hybrid orbitals this will be the case when the elements are arranged in a tetrahedral structure. Overlapping hybrid orbitals on neighboring sites produce then bonding and anti-bonding levels (C in Fig. 6), which in the solid broaden into semi-conductor valence and conduction bands (D in Fig. 6). The fact that hybridization, which is essentially a mathematical construct to change basis functions, provides a qualitative understanding of observed electronic structures in real materials is where the real value of the concept lies. In the present context, for example, hybridization can be used to rationalize the electronic structures of the group IV elements and, in particular, the qualitative trend in the size of the band gap in tetrahedral semiconductors. In C, Si, Ge, and Sn the splitting between the valence s and p shells are all around 7 to 8 eV. In the solid, however, the measured gaps between the valence and conduction bands are: C = 5.5 eV; Si = 1.1 eV; Ge = 0.7 eV; and α-Sn = 0.1 eV. This trend can be understood through sp^3 hybrid formation, which in the solid leads to sp^3 bonding (valence) and sp^3 antibonding (conduction) bands. The width of the bonding and antibonding bands, and hence the band gap, depends upon the overlap between atoms

in each solid. This is, of course, related to the "size" of the individual elements, i.e., the band gap depends on the extent of orbital overlap. Carbon (in the diamond structure) therefore exhibits the largest band gap (the strongest overlap of hybrids at adjacent atoms, the strongest cohesive energy) and α-Sn the smallest. This trend can also be captured in DFT calculations, although the quantitative value of the computed Kohn-Sham band gap depends sensitively on the exchange-correlation functional employed, which brings us to the question of the accuracy of DFT for covalently bonded elemental solids.

4.2.2 DFT for the Cohesive Properties of Elemental Covalent Solids?

As we asked before for metals, we now consider what level of accuracy to expect if we choose to perform a self-consistent DFT calculation. The properties considered are again E^{coh}, a_0, and B_0. Table 2 lists the values obtained for each of these quantities for C, Si, and Ge with the LDA, PBE, TPSS, and PBE0 functionals. As before, let's consider each functional in turn and see what general conclusions can be drawn:

(a) Like we saw for metals, LDA predicts the smallest lattice constants and the largest cohesive energies. Compared to experiment the LDA lattice constants are highly accurate. The cohesive energies are significantly larger (+14 to +22 %) and the bulk moduli straddle the experimental values (being 5 % smaller for Si and 3 % larger for C).

(b) The PBE functional predicts lattice constants that are larger than experiment (+0.7 % to +2.3 %), just as this functional did for metals. The bulk moduli are less than the experimental values (-17 % to -5 %) and the cohesive energies are within about 4 % of experiment, considerably improved compared to LDA. Note that the GGAs for solids tend to yield better lattice constants for these covalent solids but worse values for E^{coh} [39, 41].

(c) The TPSS functional appears to offer equivalent performance to PBE for lattice constants and bulk moduli. For E^{coh}, TPSS actually appears to be slightly inferior to PBE, predicting cohesive energies that are 6 to 2 % smaller than the experimental values. However, revised-TPSS does offer improvements [43].

Table II: Bulk properties of C, Si, and Ge, as computed with the LDA, PBE, TPSS, and PBE0 exchange-correlation functionals. All data is taken from Refs. [87] and [48]. Ref. [87] is an all-electron study with a Gaussian basis set. Data from ref. [48] has been obtained with the plane-wave plus PAW method. The experimental values in parenthesis have been corrected for zero point effects.

		a_0(Å)		B_0 (Mbar)		E^{coh} (eV)	
		Ref. [87]	Ref. [48]	Ref. [87]	Ref. [48]	Ref. [87]	Ref. [48]
C	LDA	3.54		4.54		8.83	
	PBE	3.58	3.57	4.22	4.31	7.62	7.71
	TPSS	3.58		4.17		7.12	
	PBE0		3.55		4.67		7.59
	expt.	3.57 (3.54)		4.43		7.37	
Si	LDA	5.43		0.95		5.26	
	PBE	5.49	5.47	0.89	0.88	4.50	4.56
	TPSS	5.48		0.92		4.36	
	PBE0		5.43		0.99		4.56
	expt.	5.43 (5.42)		0.99		4.62	
Ge	LDA	5.63		0.76		4.72	
	PBE	5.77		0.63		3.82	
	TPSS	5.73		0.66		3.78	
	PBE0						
	expt.	5.65 (5.64)		0.76		3.87	

(d) For metallic systems the hybrid PBE0 functional did not appear to offer any clear improvement over the other functionals. However, for C and Si (Ge has yet to be treated with the PBE0 functional) PBE0 does, indeed, offer slightly improved performance compared to the other functionals. PBE0 gets the lattice constants of both materials correct to within 1 %, the bulk moduli to within 5 % and the cohesive energies to within

3 % of the corresponding experimental values.

In conclusion, we again see that all functionals discussed perform reasonably well in capturing the variation in lattice constants and bulk moduli for the small collection of covalently bonded solids considered. As we observed for metals, the situation with regard to the quantitative determination of E^{coh} is far from satisfactory with the choice of exchange-correlation functional crucial to the value obtained. Finally, before closing this section we briefly discuss one further important aspect of DFT calculations of covalent elemental solids, namely how the computed band gaps compare to the experimental ones. We have indicated already that the computed Kohn-Sham band gap depends sensitively on the exchange-correlation functional used and generally it is found that the LDA and GGA functionals predict Kohn-Sham band gaps that are considerably smaller than the experimentally observed optical band gaps. The LDA and PBE band gaps of C in the diamond lattice, for example, are ∼4.2 and ∼4.8 eV, respectively, compared to the corresponding experimental value of ∼7.3 eV [48, 88]. Moving to the hybrid functionals such as PBE0 leads to increased band gaps through the inclusion of a fraction of Hartree-Fock exchange and generally (but not always) this improves the band gap compared to the pure DFT functionals. The PBE0 band gap for C, for example, is at ∼6.7 eV in much better agreement with experiment than either the LDA and PBE functionals [48].

5. Surface Structure

Knowledge of the atomic arrangement in the surface region is a prerequisite to understanding the properties of surfaces, and so let's now briefly consider the structures of surfaces. As we have said metals come most often in fcc, hcp, or bcc structures. Of the many ways to cleave such metallic crystals to produce a surface the most interesting to us here are those with low energy. These tend to be close-packed surfaces such as the (111), (100) or (110) surfaces of fcc and bcc metals, or the (001), (100), and (101) surfaces of the hcp metals. For orientation purposes we show the structures of the aforementioned fcc and bcc metal surfaces in Fig. 7. Elemental semiconductors, on the other hand, most often come in the diamond lattice. The three low-index faces of the diamond lattice are the (111), (110), and (001) surfaces, which are shown in Fig. 8. Both the (111) and (110)

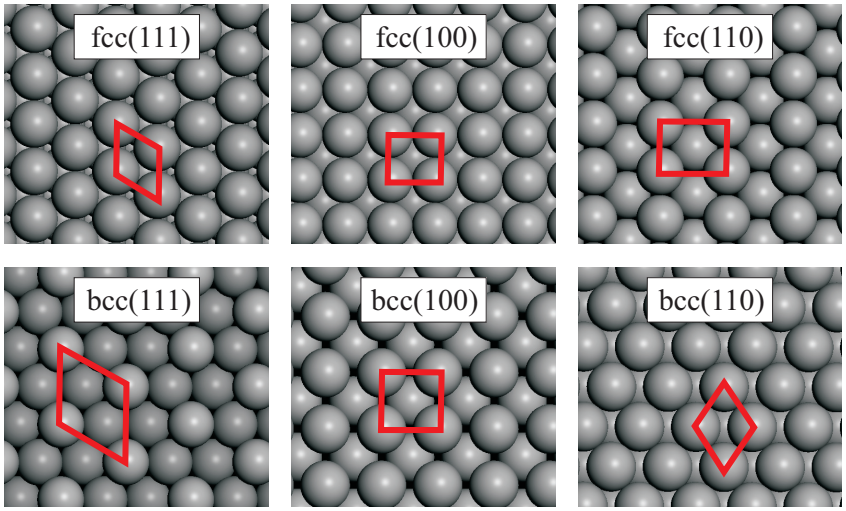

Figure 7: Structures of some bulk-truncated (i.e., unreconstructed) low Miller index surfaces of fcc and bcc metals. The surface unit cell is shown in each case. The density of surface atoms decreases from left to right for the fcc surfaces and from right to left for the bcc surfaces.

surfaces of the diamond lattice have hexagonal symmetry, whereas the (010) surface has square symmetry.

Because the atoms at the surface of a crystal have less neighbors than they do in the bulk it is unlikely that they will remain at their "bulk truncated" positions. Rather, the atoms are likely to move in response to their new environment, as discussed in great detail in Chapter I of this book. Minor displacements in which the top few layers of atoms move inward or outward along the surface normal, but retain their periodicity parallel to the surface, are generally referred to as *surface relaxations*. More pronounced alterations of the atoms in the surface region involving lateral displacements which alter their translation symmetry parallel to the surface and/or changes in the surface layer atomic density are generally known as *surface reconstructions*. We illustrate the distinction between surface relaxations and surface reconstructions in Fig. 9 and now discuss some examples of each type of behavior. In general, freshly cleaved metal and semiconductor surfaces are both liable to undergo surface relaxations and/or reconstructions. However, because making a surface in a covalent crystal involves breaking highly-directional bonds, the rearrangement of the atoms at semiconductor surfaces often involves more substantial reconstructive

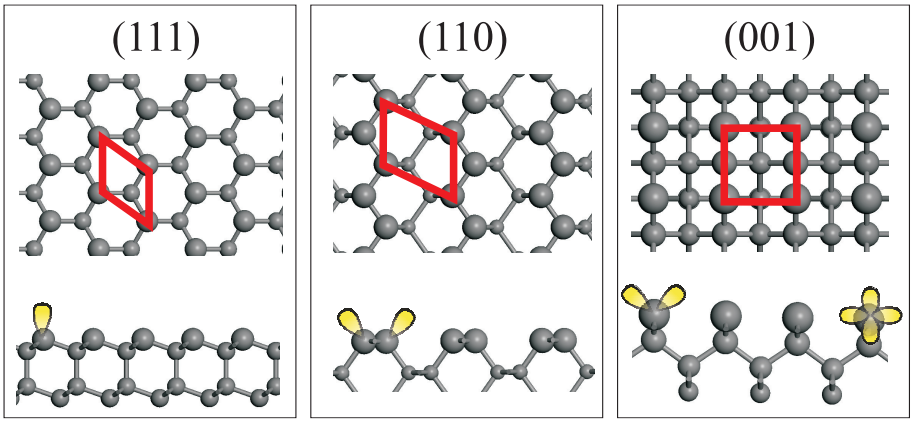

Figure 8: Top and side views of the structures of the low-index bulk-truncated (i.e., unreconstructed) surfaces of the diamond lattice. In each sub-figure the size of the atoms decreases as one moves deeper into the selvedge. The dangling bonds on the surface atoms (in a single unit cell) are also indicated. For the (001) surface the dehybridized p states are also shown on the right. Note that for the (111) surface two cleavage planes are possible. The one shown is the one that involves cleavage along two widely spaced layers (as opposed to two narrowly spaced layers), leading to a surface with one dangling bond per surface atom as opposed to three dangling bonds per surface atom.

displacements of the atoms in the selvedge as opposed to minor relaxations.

5.1 Surface Relaxation

Simple surface relaxations in which only the interlayer spacings of the top layer or so change are often observed for metal surfaces, as described in detail in Chapter I. For such systems the well-known model of Finnis and Heine is applicable and used to rationalize how the surface atoms can be expected to relax [89]. This model predicts: (i) a small *contraction* for the first interlayer spacing; and (ii) that the contraction is more pronounced for open surfaces than for close-packed ones.

The physical basis of the model is the Smoluchowski smoothing of the electron density at the surface [90]. When a crystal is cut to form a surface, the electrons rearrange in order to reduce the density corrugations and by this way their kinetic energy. This

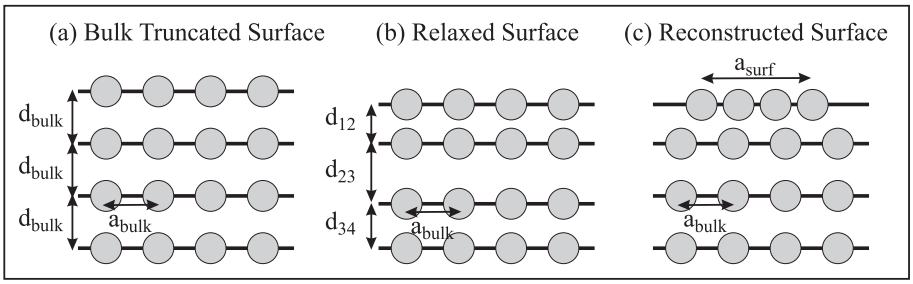

Figure 9: Schematic side views of: (a) a bulk truncated surface; (b) a relaxed surface; and (c) a reconstructed surface.

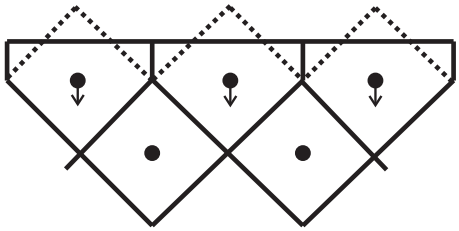

Figure 10: Illustration of the Finnis-Heine model for electron density redistribution (Smoluchowski smoothing) and interlayer relaxation at metal surfaces. See text for details (after ref. [89]).

leads to a displacement of the electrons left on top of the surface atoms downward to the crystal resulting in an electrostatic attraction of the top layer ions toward the rest of the crystal. This is illustrated schematically in Fig. 10. As electronic corrugations are rather flat for close-packed surfaces, small contractions are expected in that case. For more open surfaces larger contractions can be expected. Landman *et al.* [91] subsequently expanded the model to show that the redistribution of electronic density extends over several layers, giving rise to a tendency for a damped oscillatory nature to the relaxation. Indeed for Al(110) subsequent low-energy electron-diffraction (LEED) analysis confirmed the prediction of multilayer relaxation [92], thus representing an early success for the predictive nature of electronic-structure theories in their application to the structure of surfaces.

The model as outlined above, however, is obviously very simple and not as general as one might be lead to expect, and not as widely applicable as it is often said to be [93, 94]. In particular the closest packed hexagonal surfaces of the fcc and hcp metals often undergo an

Table III: Percentage interlayer relaxations, Δd_{ij}, for several (unreconstructed) close-packed hexagonal metal surfaces, as obtained from DFT (LDA and PBE) calculations and LEED analyses. All data is from ref. [79].

		Al(111)	Ti(0001)	Cu(111)	Pd(111)	Pt(111)
Δd_{12}	LDA	+1.35	-6.44	-1.58	-0.22	+0.88
	PBE	+1.35	-6.84	-1.19	-0.01	+1.14
	LEED	+2.2 ± 1.3	-2.1	-0.7 ± 0.5	+1.3 ± 1.3	+0.87
	LEED	+0.9 ± 0.5	-4.9	-0.3 ± 1.0	+2.4 ± 0.9	+1.20
	LEED	+1.7 ± 0.3				+1.0 ± 0.1
	LEED	+1.3 ± 0.8				+1.0
Δd_{23}	LDA	+0.54	+2.64	-0.73	-0.53	-0.22
	PBE	+0.54	+2.82	-0.65	-0.41	-0.29
	LEED	+0.5 ± 0.7	+1.4		-1.3 ± 1.3	
	LEED				+0.7 ± 0.9	
Δd_{34}	LDA	+1.04	+0.37	-0.43	-0.33	-0.17
	PBE	+1.06	-0.51	-0.24	-0.22	-0.21
	LEED		-1.1		+2.2 ± 1.3	
	LEED				+0.7 ± 1.8	

"anomalous" expansion of the first to second layer distance relative to the bulk interlayer spacing. This is clear from Table 2 where measured interlayer relaxations at a number of hexagonal close-packed metal surfaces are listed. This table includes the results of DFT (LDA and PBE) calculations and LEED analyses for simple, noble, and transition metals aiming at providing a broad and representative overview of the behavior of close-packed metal surfaces. It can be seen from the table that LEED predicts an expansion of the first to second interlayer spacing of Al(111), Pd(111), and Pt(111). For two of these surfaces (Al and Pt) there is excellent agreement between theory and experiment suggesting that the expansion is a real effect. For Pd(111) and some other surfaces not listed in Table 2, such as Rh(111) and Ru(0001), how exactly the topmost layer relaxes is still under discussion [95–99].

5.2 Surface Reconstruction

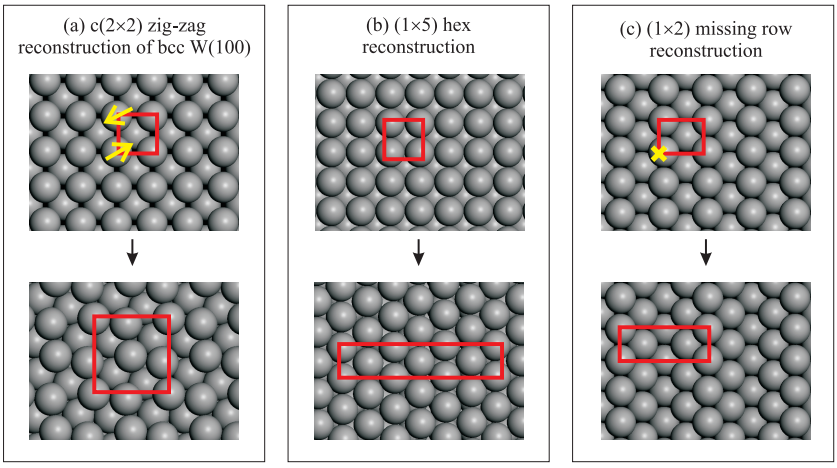

Figure 11: Illustration of three bulk truncated surfaces and typical types of reconstruction that they undergo. (a) depicts the (1×1) to c(2×2) reconstruction of bcc W(100). The arrows indicate the direction in which the top layer W atoms move upon reconstruction. (b) displays an example of the "hex" reconstruction that the late $5d$ (fcc) transition metals undergo. The specific example is the (1×1) to (1×5) reconstruction of fcc Ir(100). (c) displays the (1×1) to (1×2) "missing row" reconstruction that occurs on the (110) surfaces of the late $5d$ (fcc) transition metals. The rows of atoms removed by the reconstruction are indicated by the $\times$ at the edge of the unit cell.

For many surfaces the displacements of the atoms from their bulk truncated positions are more pronounced than a simple relaxation in which only the interlayer spacings change. These may involve lateral displacements of atoms within the surface layers and/or a change in the surface layer atomic density. First we discuss some examples of reconstructions at metal surfaces and then some examples at semiconductor surfaces.

5.2.1 Reconstructions of Elemental Metal Surfaces

In Fig. 11 we show three well-known examples of the common types of reconstructions observed for clean metal surfaces. Following Titmuss *et al.* [100] we discuss these examples as representative of three classes of reconstruction that may occur at metal surfaces:

(a) *Displacive reconstructions at constant layer density*: Some surfaces undergo displacive

intralayer lateral relaxations within the surface layers, lowering the layer symmetry but not the density. Within this class of displacive reconstructions the c(2×2) reconstruction of W(100) is the most well characterized. As illustrated in Fig. 11(a) the top layer of W atoms reconstructs from the ideal square lattice to a "zigzag" atomic arrangement. This is achieved through a pair of symmetry breaking lateral displacements as indicated by the arrows in the top part of Fig. 11(a). LEED structural analysis gives a lateral displacement of the top layer W atoms of ~ 0.2 Å [101–104]. Although not apparent from Fig. 11(a) this reconstruction also involves displacements of the sub-surface W atoms as well as a contraction of the topmost interlayer spacing of 6 %. The results obtained from DFT LDA calculations are consistent with the experimentally determined structural model and point to a coupling between one of the surface states of W(100) and a particular surface phonon mode as the origin of the reconstruction [59, 105].

(b) *Changes in surface layer atomic density*: Large-scale surface reconstructions producing changes in the surface layer density have been identified on several metal surfaces. Notably, as described in Chapter I, the top layer of the (100) surfaces of Pt, Au, and Ir reconstruct from their ideal square arrangements into quasi-hexagonal configurations known as "hex" phases [106–114]. Because of the different symmetries of the reconstructed top layer and the substrate, generally commensurate hex phases have rather long periodicities; (5×1) and c(26×68) surface unit cells have been observed [112, 113]. Indeed the (5×1) periodicity, which takes place on Ir(100), is the simplest of the hex reconstructions found and the one displayed in Fig. 11(b). Again this reconstruction involves displacements of subsurface atoms and a change in surface interlayer distances. Based on DFT calculations Fiorentini *et al.* [115] established a correlation between reconstruction and the magnitude of the surface stress and recently Havu *et al.* succeeded in performing full calculations of some of these reconstructions [114] The reconstruction arises from a balance between surface-substrate mismatch and stress-related energy gain. In the case of the $5d$ metals the latter gain is large enough to drive the reconstruction against the substrate resistance to misregistry, whereas for the $4d$ metals it is not. The origin of the surface stress was shown to be d charge depletion at the surface, caused by enhanced sp hybridization and because of relativistic effects this stress is particularly large for the $5d$ metals.

Another surface reconstruction that fits perfectly into this class of reconstructions is the so-called herring bone reconstruction of Au(111) [116–120]. Here a uniaxial contraction along one of the $\langle\bar{1}10\rangle$ directions in the top layer leads to a layer with a higher density of atoms in it than the unreconstructed (111) surface and a surface unit cell of $(n \times \sqrt{3})$ $(n = 22)$.

(c) *Missing row reconstruction of fcc (110) surfaces*: A well-known class of reconstruction is the so-called missing row reconstruction of the fcc (110) surfaces [121–125]. The (110) surface is the most open of the widely studied low Miller index fcc surfaces. Consequently, it has the lowest surface layer atomic density and the highest surface energy, making it the most likely to reconstruct. In the case of Ir, Pt, and Au the clean (110) surface spontaneously reconstructs, giving rise to the (1×2) missing row reconstruction. As the name suggests every second close-packed row along the (110) surface is removed (Fig. 11(c)), resulting in a surface comprised of ribbons of (111)-like microfacets (see Chapter I). On closer inspection, LEED as well as DFT find that each of the missing row reconstructed surfaces show all three effects discussed above: a relaxation of the first to second interlayer distance; a change in the surface layer atomic density; and a displacive reconstruction of some of the surface layers parallel to the surface. For the interested reader ref. [126] and references therein provides a more detailed discussion of this particular type of reconstruction for the specific case of Pt(110).

5.2.2 Reconstructions of Elemental Semiconductor Surfaces

This is a huge issue and one that will be covered at length throughout this and subsequent volumes. Very often elemental semiconductors exhibit a much richer variety of reconstructions than metal surfaces do [127, 128]. Fortunately, however, much of the qualitative insight into semiconductor surfaces has been condensed into a series of general principles, first laid down by Duke [129, 130] and discussed at length in several other places [128, 131]. A discussion of the relevant principles [132] along with a few examples is sufficient to provide a flavor for how some of the most-common elemental semiconductor surfaces behave.

The first principle which we discuss here is often described as the basic or guiding

principle of semiconductor surfaces and it states that *"the surface structure observed will be the lowest free energy structure kinetically accessible under the preparation conditions"*. This, rather obvious statement, is true of any surface. However, it is especially pertinent to semiconductors since which surface is observed is known to depend sensitively on cleavage, annealing, and growth conditions.

Stemming from the guiding principle are a series of other principles. Of relevance to the present discussion on elemental semiconductors is one that basically implies that a surface tends to minimize the number of dangling bonds by formation of new bonds and/or rehybridization. The concept of the "dangling" bond is absolutely key to understanding semiconductor surface reconstructions. In an elemental semiconductor, covalent bonds between neighboring atoms contain two spin paired electrons in, for example, an sp^3 hybrid orbital. When a surface is created at least one such bond per surface atom is cut, leaving some sp^3 hybrid orbitals to stick out of the surface. These orbitals are called dangling bonds. Dangling bonds are reactive and so the above principle is simply stating that real surfaces will relax or reconstruct to reduce the number of dangling bonds they possess and, in so doing, minimize the total energy of the system. Dangling bond states are surface-localized orbitals that typically reside at an energy between the valence and conduction bands. Thus these are surface states or resonances. Naturally, dangling bonds on neighboring atoms interact and so the dangling bond levels get broadened into bands. As an example we show in Fig. 12 the computed surface band structure of the unreconstructed (100), (110), and (111) surfaces of Si. These are the prototype dangling bond systems; with the dangling bonds clearly seen in the fundamental gap in each system.

The other principle relevant to elemental semiconductors (as well, by the way to the surfaces of other classes of materials) is one that states that *"...surfaces can lower their energies by atomic relaxations leading to semiconducting (as opposed to metallic) surface state eigenvalue spectra"*. Basically this principle implies that a semiconductor surface tends to be insulating or semiconducting but not metallic. In general, if there is a single dangling bond per surface atom or when two or more dangling bond bands overlap then the surface is metallic. Otherwise the surface is semiconducting. All three bulk-truncated surfaces of the diamond lattice shown in Fig. 8 are metallic and thus liable to reconstruct.

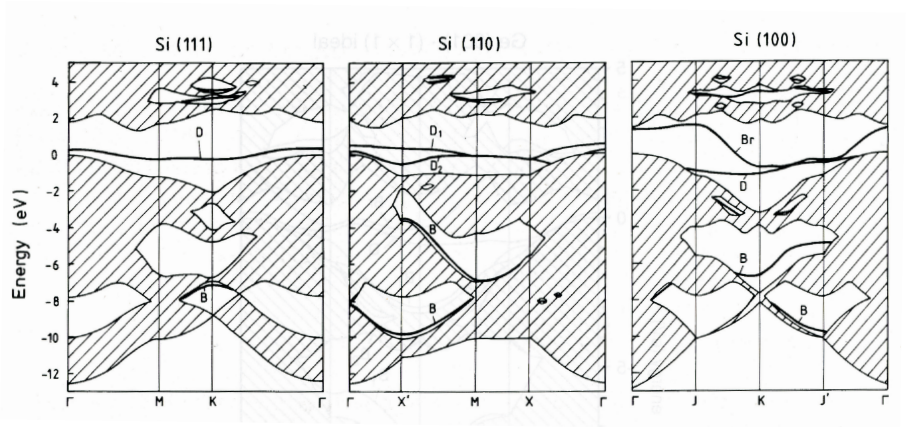

Figure 12: Surface band structures of the bulk-truncated (111), (110), and (001) surfaces of Si, as obtained from empirical tight-binding calculations (after refs. [133, 134]). The labels D, B, and Br stand for dangling bond, back bond, and bridge bond, respectively.

Let's now consider how the (001) and (111) surfaces of the diamond lattice behave. First, the (001) surface. This surface, in particular the (001) surface of Si, has been examined in detail at least as much as any other solid surface; often being described as the backbone of the semiconductor industry. The Si(001) surface undergoes a large number of reconstructions, notably to $p(2\times1)$, $p(2\times2)$, and $c(4\times2)$ phases. We discuss the (2×1) reconstruction, which is also observed for Ge and C. The atoms at the surface of the non-reconstructed (001) surface are second nearest-neighbors and each is involved in just two nearest-neighbor covalent bonds. As a result each surface atom is relatively unstable with two dangling sp^3 orbitals, as shown schematically in Fig. 8. Partly this situation is remedied through dehybridization of the sp^3 orbitals on the surface atoms back to the original atomic s and p orbitals, since lacking their tetrahedral environment the incentive to stay as sp^3 hybrid orbitals is diminished. Dehybridization leaves the surface atoms with p or sp orbitals parallel to and perpendicular to the surface, known in this specific system as bridge bond and dangling bond states, respectively. These are the states that are shown schematically on the right hand side of Fig. 13 and also the states labeled D and B in Fig. 12 Unsaturated states on neighboring atoms can interact and in so-doing further reduce the total energy of the system. Specifically this is achieved through the formation of dimers between atoms on adjacent rows. In the simplest case this gives rise to a (2×1)

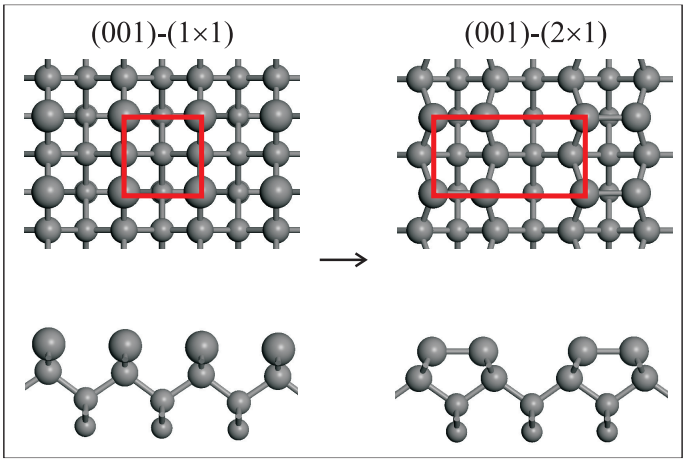

Figure 13: Left: Bulk-truncated structure of the (001) surface of the diamond lattice. Right: the (2×1) reconstruction of the (001) surface within the symmetric dimer model (SDM).

reconstruction as indicated in Fig. 13.

In Fig. 13 the dimers are parallel to the surface in a symmetric configuration known as the symmetric dimer model (SDM). However, the dimers need not necessarily lie parallel to the surface but instead may buckle or tilt. The (2×1) reconstruction comprised of buckled dimers is known as the asymmetric dimer model (ADM). For the particular case of Si(001) in the (2×1) reconstruction the question of whether the dimers buckle or not was intensely debated in the 1980s and early 1990s. It is now established that the ADM is favored for the (2×1) reconstruction on Si(001), and likewise for the (2×1) reconstruction of the (001) surface of Ge [136]. However, dynamical flipping between the two tilted orientations is pronounced even at very low temperatures [137, 138]. On C(001), however, where the orbitals are more localized and electron-electron repulsion of two electrons in the same orbital is much larger, the dimers in the (2×1) phase do not buckle and the SDM is favored [139, 140].

Important contributions to the understanding of the (001) surfaces of the group IV elements in the diamond lattice have come from DFT, including an explanation as to why the dimers buckle on Si and Ge but not on C [134, 135, 137] Specifically, by looking at the underlying electronic structures for the buckled and symmetric dimer structures, DFT reveals that on Si and Ge the buckling is required to split the energies of the dimers'

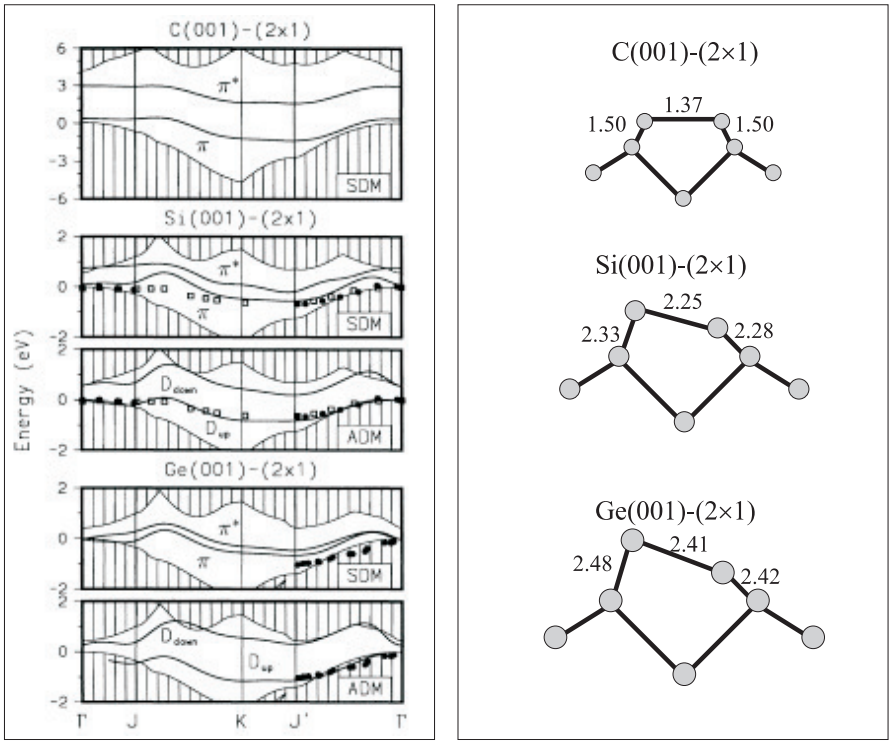

Figure 14: Left: Section of the DFT (LDA) surface band structure of C, Si, and Ge (001)-(2 × 1). The circles and squares correspond to experimental photoemission data. Right: Side views of the optimized DFT (LDA) structures of these surfaces. For C the symmetric dimer model (SDM) is favored, whereas on Si and Ge the asymmetric dimer model (ADM) is favored. Bond lengths are given in Å (from refs. [134, 135]).

bonding and anti-bonding states (in this context called the π and π^* bands) to yield a semiconducting rather than a metallic surface. For C(001)-(2 × 1) the splitting is already large enough that the surface is insulting in the SDM anyway. This can be clearly seen in Fig. 14 where partial band structures for the various (2 × 1) phases under discussion are displayed as well as details of the optimized DFT (LDA) structures of each phase. This study illustrates very clearly how with electronic structure theory it is possible to examine both stable and unstable structures and in so-doing understand the underlying physics that controls the structures which emerge. For a more detailed account of the chemical and physical differences between the (001) surfaces of C, Si, and Ge the interested reader is referred elsewhere [134, 135].

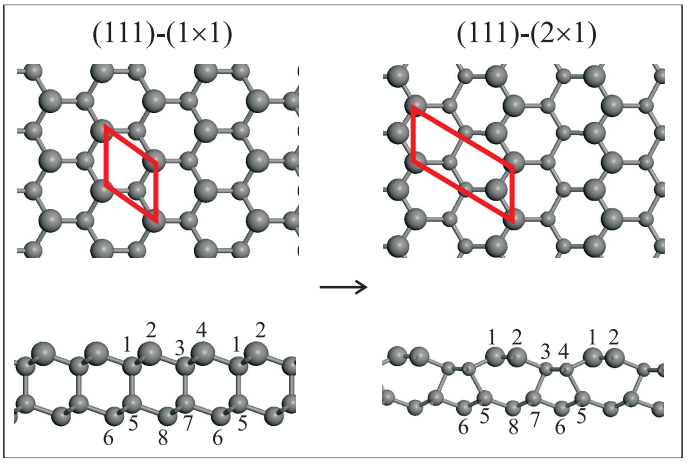

Figure 15: Left: Bulk-truncated structure of the (111) surface of the diamond lattice. Right: the (2×1) reconstruction of the (111) surface within the π-bonded chain model. Reconstruction from the (1×1) to the (2×1) structure involves cleavage of the bond between atoms 1 and 5 and the formation of a new bond between atoms 4 and 5.

Moving now to the (111) surface of the group IV elemental semiconductors. For this surface two distinct bulk-truncated terminations are possible. One involves cleavage through one of the double-layers stacked along the [111] direction of the bulk yielding a surface with three dangling bonds per surface atom. The other involves cleavage above or below one of the double layers yielding a surface with one dangling bond per surface atom. Not surprisingly the (111) termination with three dangling bonds per surface atom is less stable than the (111) cleavage plane with one dangling bond per surface atom. It is the low energy single dangling bond termination that is shown in Fig. 8 and Fig. 15.

As we have indicated already the bulk-truncated (111) surface of Si is unstable and undergoes reconstruction, notably to (2×1) and (7×7) phases. We discuss here the simpler (2×1) reconstruction and refer the interested reader to many of the other texts, including Chapter I, which describe at length the nature of the (7×7) reconstruction, which is indeed the most famous but also most complex reconstruction in surface physics (see. e.g. [128, 130, 131, 141, 142]).

The bulk-truncated (111) surface of Si is comprised of hexagonal bilayer rings within

the plane of the surface as well as 6-membered rings perpendicular to the surface. The reconstruction into the (2×1) phase involves a specific rearrangement of the bonding pattern between the surface bilayers and the subsurface atoms. With regard to Fig. 15 it can be seen how this is achieved. Specifically, the bond between the atoms labeled 1 and 5 breaks and a new one forms between the atoms labeled 4 and 5. Concomitant displacements of the atoms leave atoms 1 and 2 in the first atomic sub-layer and atoms 3 and 4 in the second sub-layer. This leaves the surface with zig-zag chains running along the $[\bar{1}10]$ direction connected to the subsurface atoms by 5- and 7-membered rings, as opposed to the 6-membered rings of the bulk structure. This zig-zag chain model for the (2×1) reconstruction of the (111) surface of the diamond lattice is known as the "π-bonded chain model ". In the original π-bonded chain model, due to Pandey [143, 144], all the top layer Si atoms in the π-bonded chains reside at the same height. However, like the situation just discussed for the Si dimers of the (100)-(2×1) reconstruction, the atoms in the π-bonded chains are liable to buckle. Specifically one can generate two analogue structures by titling the two atoms of the chain in clockwise or anticlockwise directions. How the two resulting structures, the so-called "chain-high" or "chain-left" and "chain-low" or "chain-right" structures are generated is illustrated in Fig. 16. For Ge(111)-(2×1) the anticlockwise chain-high isomer is favored. For Si(111)-(2×1) both the chain high and chain low structure are almost degenerate in energy and for C(111)-(2×1) no buckling is found. In arriving at these structures for the Si(111) surface, electronic structure theory played an absolutely crucial role by first showing that certain models were incompatible with experiment and that the new chain models had lower energies [143, 144]. For a fuller discussion focussing on the physical origin of the buckling the interested reader is referred to the book of Bechstedt [131].

5.3 Surface Structure Summary

To conclude our discussion on semiconductor and metal surface structures, these surfaces tend *not* to retain their bulk-truncated structures and a huge variety of relaxations and reconstructions are possible. The interested reader may wish to refer to Tables 2.3a and 2.3b of Somorjai's textbook on surface chemistry for a more extensive overview of the many and varied structures clean solid surfaces can adopt [93].

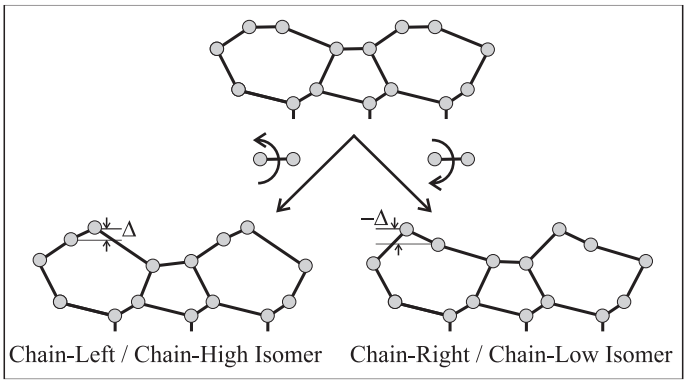

Figure 16: Side view of the π-bonded chain model for the (111) surface of the group IV elements in the diamond lattice and how it can be transformed in to two related structures known as the "chain-left" or "chain-high" and "chain-right" or "chain-low" isomers. After ref. [131].

6. Surface Energetics

6.1 Introduction and Experimental Considerations

The energy to produce a surface at a given temperature and pressure is the *Gibbs surface free energy*, G^S. The Gibbs surface free energy will be different for different facets of a crystal and is thus key to determining the equilibrium crystal shape of materials, crystal growth, surface roughening, surface segregation in alloys, and many other properties. For the elemental solids considered here, it can be defined by the relation

$$G = NG^0 + AG^S \quad , \tag{32}$$

where G is the total free energy of the finite solid, N is the number of atoms in it and A is the surface area [93, 141]. G^0 is the (reference) free energy of an atom in the idealized infinite solid. Thus G^S expresses the excess free energy that the finite solid with surfaces has over an idealized crystal comprised exclusively of bulk atoms. Excess implies that G^S is a positive quantity, i.e., it costs free energy to produce more surface. For *elemental* systems and in the absence of an applied electrical field this is always the case. For binary, ternary or more complex materials and in the presence of gas phase environments, in which the precise stoichiometry of bulk and surface phases becomes unclear, there have been

suggestions that G^S need not be positive under all conditions [145, 146].

The Gibbs surface free energy will usually be different for different facets of a crystal. Such variations, often referred to as surface free energy anisotropies, are key to determining the equilibrium crystal shape (as well as many other properties) of materials because at equilibrium a crystal seeks to minimize its total surface free energy subject to the constraint of constant volume.

To see exactly how variations in G^S impact upon the equilibrium crystal shape of materials let's now examine a simple 2D model system. Consider the schematic (cubic close-packed) crystal shown in Fig. 17(a). One can imagine different planes along which to cleave this crystal to produce a surface. Some possible cuts are indicated in Fig. 17(a) and are labeled by the angle, Θ, that they make with the [01] plane. Clearly, in this model system, cuts along $\Theta = 0°$ and $\Theta = 90°$ will yield identical close-packed surfaces, cleavage along the plane $\Theta = 45°$ will also yield a close-packed surface but with a lower density of atoms in the top layer, and cleavage along the planes $\Theta = 22.5°$ and $\Theta = 67.5°$ will produce the most corrugated (stepped) surfaces. Generally the surface energy increases with the corrugation (openness) of the surface, something we will discuss in more detail below, and thus one can expect that surfaces cut along the planes $\Theta = 0°$ and $\Theta = 90°$ will have the smallest surface energy and surfaces cut along the planes $\Theta = 22.5°$ and $\Theta = 67.5°$ will have the largest surface energy with $\Theta = 45°$ coming somewhere in between. A so-called polar surface energy plot provides a particularly convenient and concise way in which to represent the dependence of G^S on Θ, $G^S(\Theta)$, and is a useful first step towards determining the equilibrium crystal shape. In Fig. 17(b), the first quadrant of one such plot for the model system shown in (a) is displayed. Such plots are constructed by drawing radial vectors from the origin with a magnitude proportional to G^S for each value of Θ. Thus for the simple model in Fig. 17(a) the magnitude of $\overrightarrow{G}^S(0)$ is relatively small, $\overrightarrow{G}^S(22.5)$ and $\overrightarrow{G}^S(67.5)$ are relatively large and $\overrightarrow{G}^S(45)$ is somewhere in between. From such a polar surface energy plot it is then straightforward to determine the equilibrium crystal shape by applying the Wulff theorem or by, in other words, performing a Wulff construction [147]. In practice, planes (or lines in this 2D example) are constructed at the endpoints of and perpendicular to the radial G^S vectors (Fig. 17(c)). The resultant

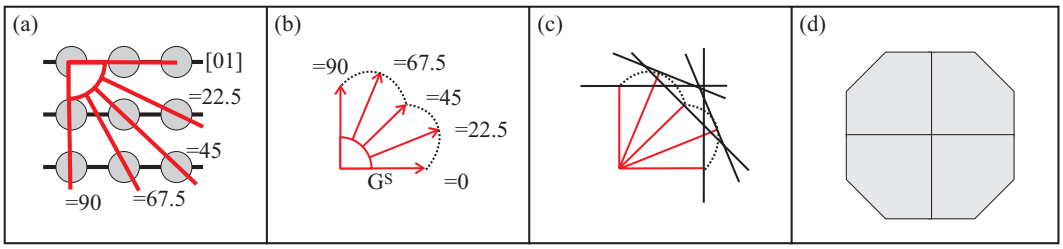

Figure 17: (a) Schematic illustration of a 2D model crystal. Several possible cleavage planes of this crystal, labeled by the angle, Θ, that they make with the [01] symmetry plane, are indicated. (b) The first quadrant of a polar surface free energy plot for the model system sketched in (a), and assuming a correlation between the corrugation of a surface and its surface energy. For each value of Θ radial vectors are drawn from the origin of the plot with a magnitude proportional to G^S at that value of Θ, i.e., the function $G^S(\Theta)$ is plotted. (c) and (d) The Wulff planes of the polar surface energy plot sketched in (b) and the resulting equilibrium crystal shape (for all four equivalent quadrants) of the model system displayed in (a).

planes (lines) are known as Wulff planes (lines) and it is simply the inner envelope - the inner Wulff envelope - of all the planes (lines) connected normal to the vectors of the surface energy plot that yields the equilibrium crystal shape (Fig. 17(d)). The resultant 2D crystal shape obtained by performing a Wulff construction on all four quadrants of a polar surface energy plot for the model system in Fig. 17(a) is shown in Fig. 17(d).

Before moving away from Wulff constructions, we briefly make a few rather self-evident but nonetheless worthwhile comments upon it. First, the distance of each face from the center of the crystal is proportional to the surface energy of that face. The equilibrium crystal shape for a purely isotropic crystal is thus a sphere. Second, the Wulff theorem can be used in "reverse", i.e., given a crystal of a particular shape one can use the Wulff theorem to extract the *relative* surface energies of the different facets exposed. This is a powerful and commonly used technique for extracting relative surface energies of different crystal facets from experiment. Third, if one cleaves a crystal along a direction which does not form part of the equilibrium boundary, the crystal will spontaneously facet along those directions that do, assuming, as always, that the system is at equilibrium. Fourth, and finally, as the volume of the crystal decreases to the nanometer scale, the accuracy of the predic-

tions one can obtain from the Wulff theorem become questionable because the energetic contribution of edges and corners at the boundary between each face becomes non-negligible.

Although the standard application of the Wulff theorem provides a means to obtain relative surface free energies from experiment, the determination of *absolute* surface free energies is, on the other hand, notoriously difficult. This is mainly because it is a small quantity and sensitive to the presence of vacancies, adatoms, steps, impurities, and kinetic barriers that prevent equilibrium structures from being attained. Interestingly, most experimental surface free energy studies from which absolute surface free energies can be obtained are indirect and old, originating in the mid 1970s and before, when the standards of surface cleanliness and perfection were unavoidably lower than they are nowadays. Although in compilations of surface energies "recommended values" may be given, one would need to be brave to make a bet of any substance on the validity of a tabulated value of a surface free energy. One need only look at published results for W, for example, to see the problem: measured values range from 105 meV/Å^2 to 281 meV/Å^2 [148].

Partly because of the difficulty in acquiring reliable surface free energies of solids, when dealing with one component systems, it is common to exploit the equivalence of G^S and surface tension, γ [149]. The surface tension, particulary the surface tension of liquids, can be determined more accurately than G^S for solids. Since it is generally believed that the surface tension of a molten liquid is about 10-20 % less than G^S for the close-packed surfaces of that solid, the liquid surface tension measurements provide what is considered an *average* surface free energy of the low-index solid surfaces. Generally these values are extrapolated on "semi-theoretical" [150] grounds to 0 K, which is how most of the tabulated surface free energy values of metals are presented [74, 150].

A notable exception to the rule that experimental surface energy measurements are old are the experiments of Bonzel and co-workers on Pb in which surface free energies for *individual crystal facets* were determined from knowledge of the temperature dependence of the equilibrium crystal shapes of Pb crystallites [151]. The Pb crystallites were supported on a Ru(0001) substrate and imaged with scanning tunneling microscopy at around room temperature and above, leading to the determination of the absolute free energy of Pb(111)

and several other low-index orientations ((100), (110), (113), (112), and (221)). Comparison of the measured value for Pb(111), 27.5 meV/Å^2 at 323-393 K, with previous recommended values of polycrystalline Pb samples show that the new value is about 15 % smaller than the previous ones. It remains to be seen where this difference comes from and if the modern value is indeed superior to its predecessor. However, DFT (LDA) calculations tend to favor the modern result [152].

6.2 Theoretical Considerations of Surface Energies

In theoretical studies, such as with DFT, the T=0 value of G^S is typically calculated, also assuming that contributions due to zero point vibrations as well as the pV term are negligible, i.e., E^S is calculated. In terms of a periodic slab calculation E^S is more conveniently defined with regard to surface area, A, as

$$G^S \sim E^S = (E_{tot}^{slab} - NE_{tot}^{bulk})/2A \quad , \tag{33}$$

where E_{tot}^{slab} is the total energy of a slab with N atoms and E_{tot}^{bulk} is the reference total energy per atom of the bulk system. The factor 1/2 takes into account the presence of two equivalent surfaces of the slab. To obtain E^s one thus needs to compute just two quantities, E_{tot}^{slab} and E_{tot}^{bulk} [153]. Before doing this one must, as always, decide on which exchange-correlation functional to trust. Since so far most calculations of E^s have been performed with LDA and GGA we restrict the comparison to just these two functionals. Comparing the results of LDA and GGA (PBE) calculations for a selection of *sp* and transition metals to the 0 K experimental data proves useful and leads to the somewhat surprising result that LDA apparently outperforms GGA (Table 3). We say "apparently", of course, because the size of the error bars on the experimental values are unclear. Nonetheless in each case GGA (PBE) predicts surface energies that are about 30 % lower than LDA, and more often than not LDA is closer to experiment than GGA. This seems to be a genuine conclusion for metals since it is also true for Pb(111) for which possibly the most reliable single-crystal surface energy measurements have been made. Here LDA comes within 2 meV/Å^2 of the experimental value, whereas GGA-PBE is about 10 meV/Å^2 lower than experiment [152].

Table IV: Theoretical (DFT LDA and PBE) and experimental surface energies in meV/Å^2 for some close-packed transition metal surfaces. All data is taken from ref. [79] except for the Pb results which are from ref. [152].

	Mg(0001)	Al(111)	Ti(0001)	Cu(111)	Pd(111)	Pt(111)	Pb(111)
LDA	38.7	56.8	141.7	119.8	116.7	139.2	26.0
PBE	35.0	46.8	124.2	88.0	83.0	104.2	17.2
Exp.	49.3	71.2	124.2	114.2	125.5	155.4	27.5

Studies on jellium surfaces provide a partial explanation for why LDA outperforms GGA for the calculation of the surface energy of metals. Specifically they show that the exchange-correlation contribution to the surface energy is calculated more reliably with the LDA due to a favorable cancelation of errors: LDA overestimates the exchange contribution to the surface energy, but underestimates the correlation contribution, whereas PBE underestimates both quantities [154–156]. Since these results on jellium surfaces are apparently transferable to real metals, it is reasonable to anticipate that functionals which are superior to LDA for jellium surfaces will also be superior to LDA for real metal surfaces. In this regard it appears that the meta-GGA TPSS, PBE-WC, and a functional from Mattsson and co-workers based on a subsystem functional approach offer some promise [37, 156, 157]. However, whether these functionals live up to expectations for real metal surfaces and solid surfaces in general remains to be seen.

6.3 Phenomenological Theories of Surface Energies

So far we have not discussed the physics of the surface energy. Why do different materials exhibit different surface energies? Why does the surface energy of different facets of the same material differ? Essentially both questions are the same as asking: what controls the magnitude of the surface energy? The qualitative answer to this is very simple: *the surface energy is related to the number and strength of the bonds per unit area which are broken in creating the surface.* Thus surface energies exhibit similar dependencies over the periodic table (e.g. from Y to Ag) as cohesive energies do, and surface energies are lower for more closely packed surfaces than they are for the more open ones or with less dangling

unsaturated bonds.

(a) Surface energies and cohesive energies

For any given element its surface energy is a fraction of its cohesive energy. Often it turns out that G^S *per surface atom* $\sim 1/6E^{\mathrm{coh}}$ per bulk atom [158]. The surface dependance comes in via the number of atoms at the surface or unit area. This rough empirical relationship can be seen in Fig. 18(a), for example, where the ratio of experimental heat of vaporization and experimental surface energy is plotted for more than 20 metals. Correlations like this have a long history and can easily be refined to account for the elements which are outliers on the plot [159].

So where does the value of the proportionality constant come from? Simply counting the number of nearest-neighbor bonds that break in making a close-packed surface would lead one to expect a value of 1/4 or larger, since at the most closely packed (111) surface of an fcc metal 1/4 of the bonds are broken. On less closely packed surfaces obviously more bonds are broken. As discussed by Methfessel *et al.* [161, 164] the reason the simple bond cutting model fails to predict the correct proportionality constant is that it neglects to account for the variation of the bond strength with coordination number, C. In particular it must be recognized that bonds between an atom with a few neighbors are stronger than those between an atom with many neighbors. This coordination-number-bond-strength relationship is well known and has, for example, been calculated explicitly with DFT for several metals, showing that the energy per bond can be as much as twice as large for $C = 2$ compared to $C = 12$ [164, 165]. Since making an fcc (111) surface entails cutting the comparatively weak twelfth, eleventh, and tenth bonds, the overall cost to make the surface is less than would be predicted by the simple linear bond cutting concept.

The coordination-number-bond-strength relationship is qualitatively captured in simple tight-binding schemes in which the energy per bond can be assumed to scale with $\sqrt{C}$ leading to

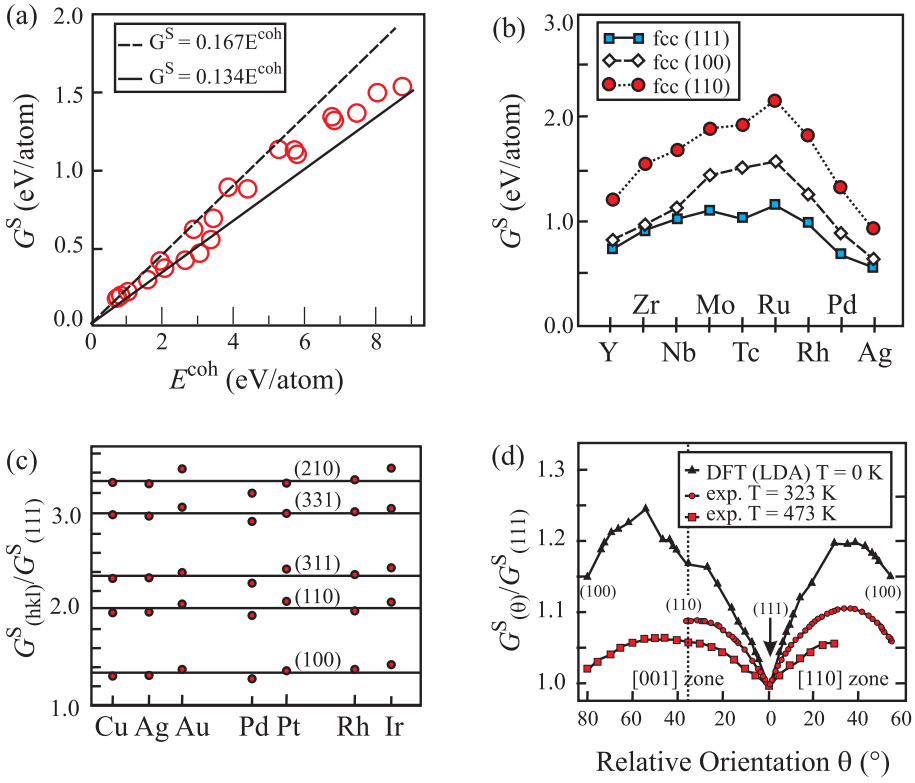

Figure 18: (a) Plot of experimental values of the surface free energy (G^S) (from ref. [150]) against the cohesive energy ($E^{\rm coh}$) (from ref. [160]) for more than twenty simple, transition, and noble metals. Lines corresponding to proportionality constants of 1/6 and the result of eqn. (34), 0.134, are also displayed. (b) Variation of the computed DFT LDA surface energies across the $4d$ transition metal series and for various close-packed surfaces. Note that in this plot fcc crystals have been used for all metals (after ref. [161]). (c) Computed DFT anisotropy ratios, relative to the (111) surface, for the low index and the most close-packed vicinal surfaces of some noble and transition metal surfaces (after ref. [162]). (d) Plot of experimental (two lower curves) and theoretical (upper curve) anisotropy ratios, relative to the (111) surface, along the [001], [$\bar{1}$10] and [01$\bar{1}$] zones for a series of Pb surfaces (after ref. [163]).

$$E^S = \frac{\sqrt{C^{bulk}} - \sqrt{C^{surf}}}{\sqrt{C^{bulk}}} E^{coh} \quad , \tag{34}$$

where C^{bulk} and C^{surf} are the coordination number of the bulk and the surface, respectively. For an fcc (111) surface eq. (34) yields a surface energy per atom of $0.134E^{\rm coh}$ which gives results rather close to the ones plotted in Fig. 18(a). Refinements of the

tight-binding treatment to account for repulsive forces between the atoms improves the agreement with experiment further [161, 164].

(b) Surface energy anisotropy

As we have said the variation of surface energy with the type of crystal facet exposed is known as surface energy anisotropy. Generally it is known that the surface energy of a material is proportional to the number of broken bonds at the surface. Thus more open surfaces with more under-coordinated atoms (i.e., more broken bonds) are less stable than the close-packed ones. This effect is qualitatively seen in the equilibrium crystal shapes of materials which expose close-packed surfaces at the expense of more open ones. First principles theory provides a considerable body of quantitative support for this concept [88, 131, 152, 161–164, 166–168]. As an example we show in Fig. 18(b) the computed DFT LDA surface energies of Methfessel *et al.* [161, 164] for model fcc (111), (100) and (110) surfaces of the 4*d* transition metals. Clearly for each metal the surface energy increases along with the corrugation of the surface, being lowest for the (111) surfaces and highest for the (110) surfaces.

More recently Galanakis *et al.* [162, 167] have shown that for the surfaces of several fcc metals there is an almost perfect linear correlation between the *relative surface energies* of different crystal facets and the number of broken bonds. This is shown in Fig. 18(c) for a number of fcc transition metal surfaces. Precisely the DFT LDA computed anisotropy ratios (relative to the (111) surface) for the (100), (110), (311), (331), and (210) surfaces of several transition metals are displayed. The solid horizontal lines are the ideal broken-bond ratios, which for the (100) surface, for example, is 4/3 since each atom on this surface has only 8 nearest neighbors compared to 9 in the (111) surface. It can be seen that in every case the computed results fall on the ideal lines or within a few percent of them. Calculations on other fcc metal surfaces, including an extensive series of 35 Pb surfaces and a large set of Cu surfaces predict that this trend also applies to these substrates; typically computed surface energies were within 5 % of what would be predicted from the broken bond rule [163, 168]. It has been argued that the linear correlation in the *relative* surface energies is not inconsistent with eqn. (34) and the basic knowledge that the binding energy

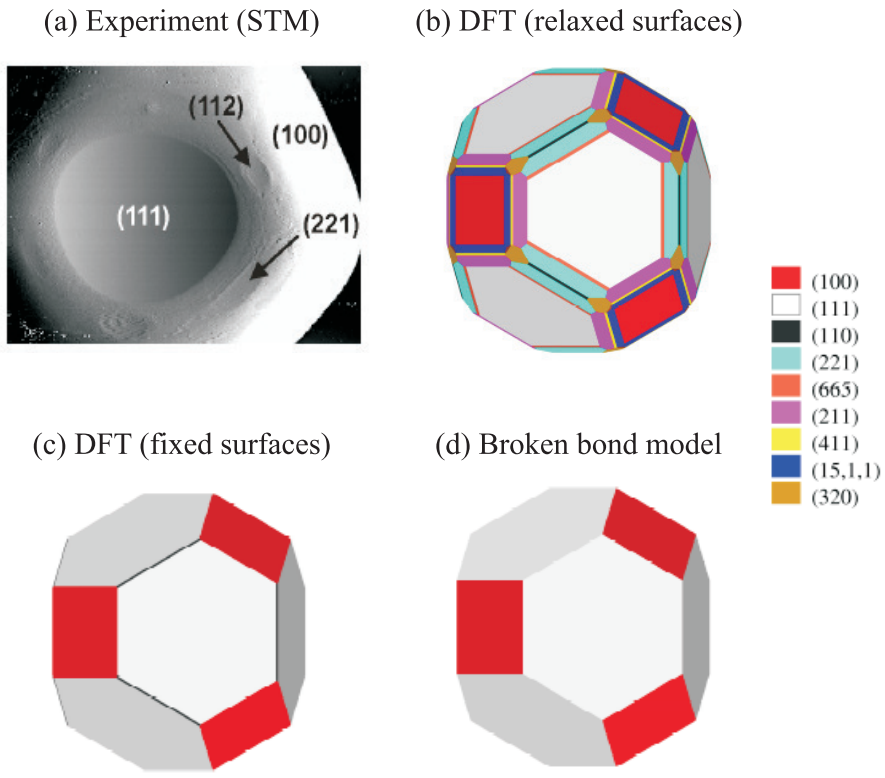

Figure 19: (a) Scanning tunneling microscopy (STM) image of part of a Pb crystallite showing the (111) and the surrounding 2-fold symmetric (221) and (211) facets as well as a (100) facet at the contact edge to the substrate. The image size is *ca.* 970 × 750 nm. (b)-(d) Three dimensional equilibrium crystal shapes of Pb constructed from DFT LDA surface energies. (b) is obtained from computed surface energies on relaxed surfaces, (c) from computed surface energies on fixed surfaces, and (d) with the vicinal surface energies obtained from the linear broken bond model (after ref. [169]).

does not scale linearly with coordination number C, by recalling that the square root in eqn. (34) can be linearized in the regime of high coordination [162].

Recent experimental results on Pb crystallites [151, 170, 171], provide valuable data with which to assess the validity of the trends predicted by DFT. Summarizing an extensive series of comparisons between experimental and DFT results [152, 163, 169, 172], it is found that the surface energy anisotropies obtained from experiment and predicted by theory agree with each other reasonably well. In Fig. 18(d), for example, the experimental

and theoretical surface energy anisotropies are plotted along the [001], [$\bar{1}$10] and [01$\bar{1}$] zones. At 323 and 473 K the experimental anisotropies are 11 and 6 %, respectively, whereas the T = 0 K theoretical anisotropy is at 25 %, expectedly higher than the finite temperature experimental values. In addition the directions of the maxima and minima of the theoretical anisotropy curve coincide with the experimental values. Moreover, when the theoretical equilibrium crystal shape - obtained by performing a Wulff construction with the theoretical surface energies - is compared to experiment, the qualitative agreement is good. As shown in Figs. 19(a)-(b) many features of the experimental equilibrium crystal shape are reproduced by the theoretical one, such as the 3-fold symmetry of the central (111) facet and the smaller peripheral (211) and (221) facets. Also shown in Figs. 19 are the predicted equilibrium crystal shapes obtained from the surface energies of unrelaxed Pb surfaces (Fig. 19(c)) and from the application of the linear broken bond rule. It is clear that the equilibrium crystal shapes obtained with the alternative data sets differ noticeably from experiment. In particular the assumption of a linear dependence of the surface energy with the number of broken bonds results in an incorrect crystal shape with just the low-index (111) and (100) surfaces present. Thus although approximate linear correlations are observed between the surface energy and the number of broken bonds the deviations from linearity are essential for a correct description of the equilibrium crystal shape.

7. Surface Electronic Structure

Let's now consider how the electronic structure at the surface differs from that in the bulk. We have already seen for semiconductors that the loss of translational symmetry along the surface normal has important consequences for the electronic structure, notably through the formation of dangling bonds which, as we have seen, have profound implications for the surface structures that form. Now we focus on the electronic structures of metal surfaces and take this as an opportunity to discuss important concepts such as the surface dipole, the work function, surface core level shifts, and surface states. First we look at the surfaces of simple metals, where we find that again jellium provides useful insight, we then move on to the transition metals and tight-binding arguments.

7.1 Jellium Surfaces: Electron Spillout; Surface Dipole; and Work Fnction

Take the jellium model that we introduced earlier for the infinite crystal and terminate the positive background (n_+) abruptly along a plane at $z = 0$, with the positive uniform background now filling the half-space $z \leq 0$ with the form:

$$n_+(z) = \overline{n}, z \leq 0$$
$$= 0, z > 0 \tag{35}$$

where $\overline{n}$ is the mean density of the positive charge in the ionic lattice. For a range of densities ($r_s = 2 - 6$) Lang and Kohn [173, 174] considered how the density (within the LDA) would behave at such an interface. The now famous plot displayed in Fig. 20(a) was obtained, which shows that: (i) the electron density spills into the vacuum; and (ii) the density within the boundary oscillates in a Friedel manner with an amplitude that decreases asymptotically with the square of the distance from the surface. The characteristic wavelength is one half of the Fermi wavelength, k_F, where $k_F = (3\pi^2 n)^{1/3}$ [175]. The amount of spillout into the vacuum and the amplitude of the Friedel oscillations depends on the Wigner-Seitz radius r_s. The smaller r_s is, the larger the spillout. The larger r_s is, the greater the amplitude of the oscillations.

The potentials associated with such density distributions are sketched in Fig. 20(b). In particular the total effective (Kohn-Sham) potential, V^{eff}, and the electrostatic potential, V^{es} are plotted. The difference between them is the exchange-correlation contribution to the total effective potential which one can see comprises the largest part of V^{eff}. This is generally true for low and intermediate densities. Two aspects of the potentials are worth commenting upon. First, as a result of the local-density approximation, V^{eff} vanishes exponentially into the vacuum. This asymptotic behavior is not correct. Instead, since as an electron moves out of a metal surface its exchange-correlation hole stays behind, flattening out on the surface, the effective potential should follow an image-like form at large z:

$$V^{\text{eff}}(z) = \frac{1}{4|z - z_{image}|} \quad . \tag{36}$$

Here z_{image} is the so-called image plane, which for many purposes is considered the "effective surface plane" [141, 176]. For typical values of r_s the image plane (from LDA

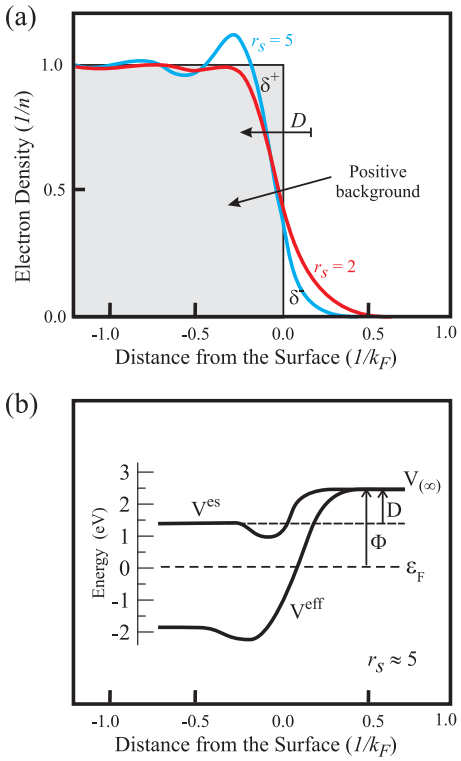

Figure 20: (a) Self-consistent electron-density distributions at a jellium surface for r_s=2 and r_s=5. (b) Schematic illustration of the potentials that develop at the jellium surface within the local-density approximation for an $r_s \sim 5$. All symbols are defined in the text (after ref. [173]).

predictions) of clean jellium surfaces resides about 2-3 Å to the vacuum side of the positive uniform background ($z = 0$) [176]. As we will see, however, the LDA error in the asymptotic behavior of $V^{\rm eff}$ has little effect on the properties of interest here such as the ground-state electron density and work function which are determined largely by the position and height of the potential rather than its detailed shape.

The second feature of the potentials sketched in Fig. 20(b) that we comment upon is $V^{\rm es}$, the electrostatic potential. Although $V^{\rm es}$ is a relatively small component of the barrier, it is of the utmost importance since it is closely related to the work function, Φ. V^{es} arises because the spread of electrons beyond the edge of the positive background renders the electrostatic potential in the vacuum, $V^{es}(\infty)$, higher than that in the metal interior, $V^{es}(-\infty)$. (For a real system "∞" means large compared to the lattice constant but small compared to the crystal dimension.) Thus an electron trying to leave the metal encounters

an electrostatic surface dipole layer, D, with an electrostatic potential energy difference of height

$$D = V^{es}(\infty) - V^{es}(-\infty) \quad . \tag{37}$$

From Poisson's equation this can be written as

$$D = 4\pi \int_{-\infty}^{\infty} z[n(z) - n_+(z)]dz \quad . \tag{38}$$

This integral across the surface boundary is obviously an electric dipole, the surface dipole, which is related to the work function, Φ, through

$$\Phi = D - \mu \quad , \tag{39}$$

where μ is the electron chemical potential, which in a metal at 0 K is equal to the Fermi level (as discussed in section 4). Thus we arrive at the definition of the work function as the minimum work necessary to remove an electron from a metal at 0 K [177].

Clearly the more the electrons spill into the vacuum, the larger D is. Indeed Φ generally increases with decreasing r_s as is illustrated by Fig. 21(a) where the work function of jellium is plotted as a function of r_s along with several experimental values for polycrystalline metals. It can also be seen from the plot that the trend predicted by jellium is indeed observed with experimental measurements on real crystals. Moreover, the absolute values of Φ predicted with the jellium model fall in the range 2-4 eV and come within 10-20 % of experiment for each of the *sp* metals listed.

A similar reasoning, although with the necessary introduction of a crystal lattice, explains the well-established fact that for real crystals, Φ can differ from one facet to the other, a concept known as work function anisotropy. For example, the measured values of Φ for the (111), (100), and (110) surfaces of Cu are 4.74, 4.64, and 4.52 eV, respectively [74]. Since μ or E_F in eqn. (39) is a bulk quantity the anisotropy in Φ comes directly from the different dipoles established at the different surfaces. Generally it is known that the more open a surface, the smaller D is and consequently the smaller Φ is, as we see for Cu above. Obviously, for jellium D is the same for all surface orientations. However, for a

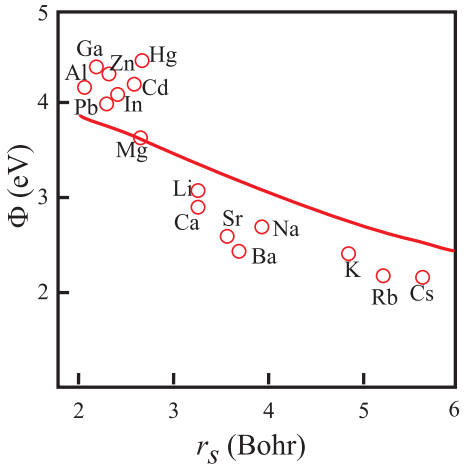

Figure 21: Computed work function of jellium as a function of r_s along with measured experimental values for polycrystalline surfaces (after ref. [174]).

real crystal, say fcc, the electron density is quite smooth at the (111) surface getting more corrugated at the more open surfaces. In the latter situations the electron density will smoothen out parallel to the surface to lower the kinetic energy (Smoluchowski effect), and as a consequence the surface dipole moment will be reduced compared to that of the closer packed surfaces.

7.2 Transition Metal Surfaces: Band Narrowing and Surface Core Level Shifts

As we know tight-binding arguments are more appropriate than jellium when seeking to gain qualitative insight of transition metal surfaces. In tight-binding language the surface suppresses a certain number of hopping integrals, since the surface atoms have lost some neighbors in any sphere of coordination. This reduces the average width of the PDOS on a surface atom relative to the bulk. Such "band narrowing" is a general phenomenon of solid surfaces when the valence states are comprised of localized orbitals such as the d valence orbitals of the transition metals. The bands of the surface atoms cannot narrow without consequence, however. Given that the whole metal has a single Fermi level, narrowing alone would lead to an unrealistic lack or surplus of electronic charge on the surface atoms depending on the filling of the band. To avoid (or to at least reduce) this the center of gravity of the narrowed bands shift; either up or down in energy. The magnitude and direction of

the shift, Δ_S, can be approximated with the rectangular d band model introduced earlier, and is given by,

$$\Delta_S = E_F(1 - \sqrt{\frac{C_{surf}}{C_{bulk}}}) \quad , \tag{40}$$

where, as before, C_{bulk} and C_{surf} are the coordination numbers of atoms in the bulk and at the surface, respectively. The energy zero in eq. (40) is the center of the bulk d band, E_d, and thus within this simplified model Δ_S is negative for less than 1/2 filled bands, positive for more than 1/2 filled bands, and zero for an exactly half filled band. We illustrate schematically the essence of this model in the upper part of Fig. 22. It is also worth pointing out that since Δ_S increases with the number of broken bonds at the surface, the more open the surface, the larger the shift, and naturally as one descends into the bulk of the crystal the bulk value for the band width is immediately recovered (within the model).

The qualitative behavior predicted from the rectangular d band model can actually be seen in self-consistent DFT calculations, where the shape of the DOS is explicitly calculated. For example, we show this in the lower part of Fig. 22 where the bulk and surface PDOS projected on to the valence d orbitals is plotted for bulk Zr and Ru and for Zr and Ru (0001) surfaces. For both Zr and Ru the d PDOS associated with the surface atoms is narrower than that of the bulk. For Zr with < 5 d electrons the surface d PDOS moves down in energy (~ 0.1 eV) relative to the bulk, and for Ru with > 5 electrons the surface d PDOS moves up in energy (~ 0.3 eV) [178].

Of more significance, perhaps, is that the shifts in the valence levels correlate with shifts in the core electrons and that the latter are now accurately and routinely measured with x-ray absorption spectroscopy (XPS) [93, 179, 180], as described in Chapter I. Such shifts in the core electrons, known as surface core level shifts (SCLS), have been measured on many close-packed transition metal surfaces finding the same qualitative trend illustrated in Fig. 22 for the valence states, i.e., a shift to deeper binding energies is observed for elements to the left of the transition series and a shift to shallower binding energies for elements to the right. Quantitatively the core level shifts differ from the d-band shifts. See, for example, refs. [179, 181, 182]. Surface core level shifts can also be computed within the framework of DFT. However, to ensure good agreement with experiment it is often necessary to put

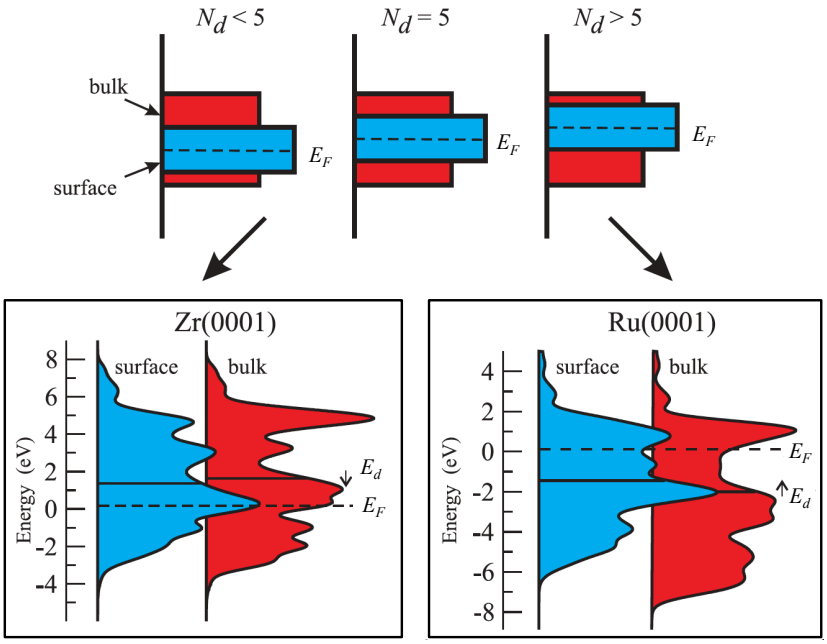

Figure 22: Upper part: schematic illustration of d-band narrowing at transition metal surfaces and its consequence for the energy levels of the surface atoms with less than 5 d electrons ($N_d < 5$), exactly 5 d electrons ($N_d = 5$), and more than 5 d electrons ($N_d > 5$). Lower part: PDOS for the d orbitals in bulk Zr and Ru and at the surface of Zr(0001) and Ru(0001), as computed within the LDA. E_d is the center of gravity of the d PDOS and the small arrows indicate that E_d is lower at the surface than in the bulk for Zr whereas E_d is higher at the surface than in the bulk for Ru (computed by the authors).

in a little more effort with the DFT calculation than simply computing the differences in the eigenvalues of core electrons at the surface and in the bulk, as was done for the valence DOS (Fig. 22). Consider what is actually measured in a core-level photoemission experiment: It is the difference in the energy it takes to remove a core electron from an atom at the surface and from an atom in the bulk. From this definition it follows directly that the SCLS of a particular core level is the difference in the self-consistent total energy between a sample with a core hole at the surface compared to the core hole being in a bulk atom. This binding energy shift thus includes changes in the core orbital energies between bulk and surface atoms *and* differences in the screening of the core hole created by the different surroundings of the core hole at the surface and in the bulk of the material. The former effect is typically called the "initial state" contribution, whereas the latter is

called the "final" state contribution. The inclusion of such "final state" effects can often be necessary if quantitative agreement between experimental and theoretical values of SCLS is sought [182–185]. In some cases it can even affect the qualitative physics [182, 186].

7.3 Surface States

As we have seen the electronic structure of metal surfaces is likely to differ from that in the bulk. One way this altered behavior is exemplified is through the formation of so-called surface states [187–190]. The surface states of metals represent interesting physical phenomena in their own right, as examples of confined two-dimensional electronic systems, but can also affect the physical and chemical properties of metallic interfaces, playing, for example, a role in the mediation of adsorbate lateral interactions [191–193]. They are routinely observed in experiment, notably with angle-resolved photoemission spectroscopy (ARPES) or with scanning tunnelling microscopy [194, 195] (also see Chapter I).

Consider a wavefunction in the bulk as it approaches a metal surface. If it is reflected back into the bulk and decays exponentially into the vacuum it is a bulk state (Fig. 23(a)). Certain bulk states may have a larger weight at the surface than in the bulk unit cell. Generally these are referred to as surface resonances (Fig. 23(b)). However, other wavefunctions may be localized almost exclusively at the surface and decay exponentially into the bulk as well as into the vacuum (Fig. 23(c)). These electronic states localized near the surface are surface states, and can be defined more precisely as states that occur in "forbidden" [196] regions of the bulk band structure, i.e., at an energy and $k_{\|}$ value or point-group symmetry for which there are no bulk states into which they can decay. This implies that surface states appear in "gaps" of the bulk band structure. Even though metals do not (by definition) exhibit *absolute* band gaps there can be many regions of $\boldsymbol{k}$-space for which at specific energies there are no states. For example, in the bulk band structure of Cu (Fig. 4(a)) there are no states above the d band until well above E_F along the path $\Gamma \rightarrow L$. Thus this represents a potential region in which, given the appropriate conditions, a surface state may appear. Indeed the (111) surface of Cu is perpendicular to the $\Gamma \rightarrow L$ path and, as we will see, a surface state does indeed reside in this region of the surface projected bulk band structure of Cu(111).

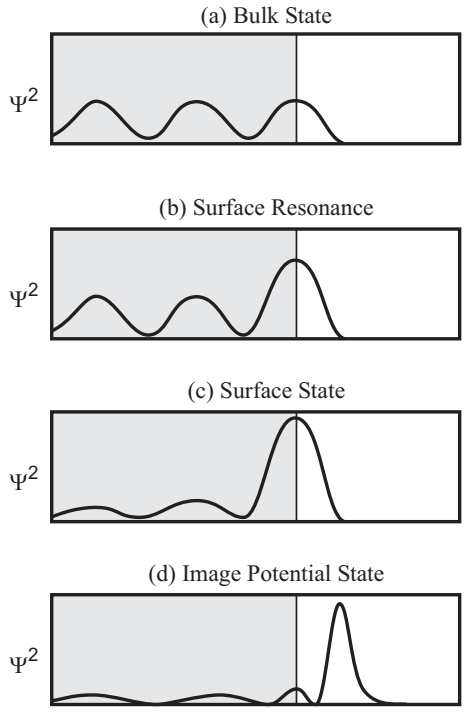

Figure 23: Schematic illustration of: (a) an idealized bulk state; (b) an idealized surface resonance; (c) an idealized surface state; and (d) an idealized image potential state.

Surface states are usually classified as Shockley [196] and Tamm states [197], and we now briefly discuss these two types of surface state in turn. However, we caution in advance that while useful the distinction is somewhat arbitrary since both types of state describe the same physical phenomenon of a wavefunction that is localized at the surface and decays exponentially into the bulk (also see Chapter I).

(a) *Shockley states:* These are typical of the simple and noble metals. Indeed the hexagaonal close-packed surfaces of Be, Mg, Al, Cu, Ag, and Au all possess an occupied Shockley state [198]. They arise simply because the presence of the surface allows solutions of the Schrödinger equation which would otherwise be imaginary in the bulk to become real in the semi-infinite crystal. Shockley states appear close to the low energy (i.e., high binding energy) border of a gap and reveal a free-electron-like behavior parallel to the surface. A particularly well characterized Shockley state is the one that occurs on Cu(111). According to ARPES this is a free electron-like state which at the $\overline{\Gamma}$ point of the surface

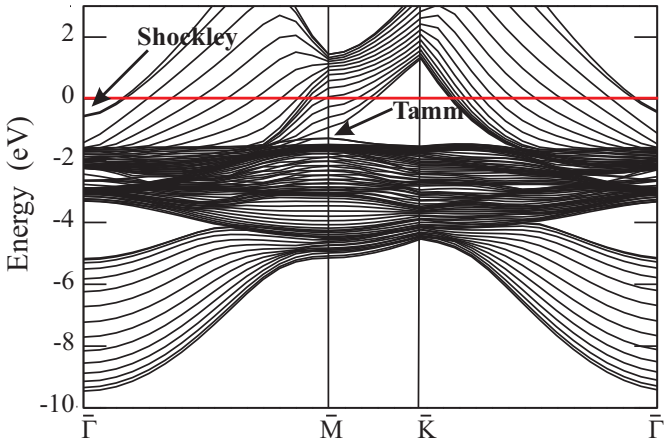

Figure 24: Surface projected bulk band structure for a 12 layer Cu(111) slab as computed from a plane-wave pseudopotential DFT calculation within the LDA (computed by the authors).

Brillouin zone resides $\sim$ 0.4 eV below E_F [199, 200]. DFT calculations agree with this finding, as can be seen from the computed band structure of Cu(111) shown in Fig. 24. The Shockley state can be seen at the $\overline{\Gamma}$ point just below E_F.

(b) *Tamm states:* These are characteristic of more tightly bound systems such as the transition metals in which the valence electrons are d states. Tamm states are split-off states due to the reduced atomic coordination of the surface and the weaker potential that arises (which was discussed in section 7.2). They reside also at the low energy border of gaps and often exhibit negative effective masses. Noble metal surfaces such as Cu(111) also exhibit Tamm states (in addition to Shockley states) and indeed in Fig. 24 an occupied Tamm state 1.8 eV below E_F can be seen at the $\overline{M}$ point split off from the top of the Cu d band. Again the computed value of this surface state agrees with experiment [201, 202].

Finally we mention yet one more type of state that can occur at metal surfaces, these are so-called image potential states which are localized mostly in the vacuum region of the metal surface (Fig. 23(d)). Recall from section 7.1 how the image potential rises to the vacuum level V_∞ as one moves out from the surface into the vacuum (Fig. 20(b)). This potential can actually support *unoccupied* bound states, i.e., image potential states. These states lie above the Fermi energy, in a Rydberg-like series of states converging

towards the vacuum level. Concerning image potential states, in particular, and surface states, in general, the reader is referred to Chapters I, X.., X as well as to the book by Davison and M. Stęślicka [187] or some of the excellent reviews on these topics [190, 203, 204].

8. Conclusions and Perspectives

Due to the broken symmetry normal to the surface and the reduced coordination it is fair to assume that the physical properties at the surfaces are different from those in the bulk of a solid. By now, much is known about these peculiarities of clean surfaces. In many cases we know where the atoms are, where the electrons are, and how stable both the atoms and electrons are at their chosen locations. We have seen how at some surfaces the atoms rearrange to form complex structures not known elsewhere in nature, whereas at other surfaces the atoms remain happily at their bulk-like positions. We have seen how electrons literally spill out of some surfaces, whilst at others they become trapped finding it almost impossible to escape. We have seen how at some surfaces the electrons sense the presence of the surface by moving up in energy, at others they move down, and at yet other surfaces they do nothing, apparently oblivious to their reduced coordination compared to the bulk. And, we have seen that the cost in energy to produce some surfaces is high, to produce others it is low, and the balance between them conspires to yield a rich variety of equilibrium shapes for crystals. This body of knowledge comes from countless surface science experiments over the last 30-40 years, using all the fine experimental methods addressed in this book. Theoretical studies, a number of which we have mentioned, nowadays are not only able to reproduce the experimental findings on the basis of fundamental principles, but have also reached an impressive level of predictive power. In particular, we have focused mainly on the contributions from density-functional theory, although the qualitative insight obtained from simplified tight-binding schemes should not be overlooked [76, 205].

Let's now recap some of the key points made in this chapter and which will be treated in great detail in the remainder of this volume. Further we outline a few challenges and issues that remain to be addressed in future work.

(a) *Surface structures:* Atoms at clean surfaces generally do not maintain their bulk-

truncated positions. Relatively simple *relaxations* in which the interlayer spacings in the surface region are modified are common for metals, as are more complex *reconstructions* in which the atoms in the surface region undergo lateral displacements, experience a change in atomic density, or change in bonding topology. Metal surfaces exhibit a rich variety of reconstructions and semiconductor surfaces an even richer variety.

In most cases the results of DFT calculations, even with exchange-correction functionals as simple as the LDA or GGA, and LEED analyses agree on the structural details of a particular relaxation or reconstruction. Further, DFT can generally provide an adequate *a posteriori* explanation for why a relaxation or reconstruction take places, such as for the hex phase of the late $5d$ fcc transition metals. However, there are several surfaces where discrepancies persist and further attention from experiment and theory alike is needed.

(b) *Surface energetics:* The most fundamental energetic quantity of a surface is the Gibbs surface free energy. This controls the surface that is stable under conditions of constant temperature and pressure. Trends in the Gibbs surface free energy have been discussed, as have variations across different types of surface. The statement that the surface energy is proportional to the number and strength of the bonds which are broken in creating the surface has been shown to be qualitatively correct.

Demonstrably reliable and quantitatively correct experimental surface energies are however generally lacking. The recent STM-based experiments for Pb are a welcome development. There is a pressing need for more measurements of this kind.

(c) *Surface electronic structures:* The concept of the dangling bond at semiconductor surfaces has been introduced and the inextricable link between dangling bonds and semiconductor surface structure emphasized. The general qualitative behavior of the ground-state electronic structure at metal surfaces has also been addressed. Much of this qualitative insight comes from the pioneering studies of Lang and Kohn on jellium surfaces and the semi-empirical tight-binding studies discussed briefly here and covered in more detail elsewhere [76]. The former provide the basis for understanding the physical origin of the work function and trends in the work function from one metal to another. Whereas the

latter are helpful for understanding concepts such as band narrowing and surface core level shifts.

Further Reading

Aside from the many original articles, review papers, and books cited already, the interested reader may wish to consult the following texts for complimentary and in some cases more detailed discussions on the physical and chemical properties of solid surfaces:

- *Physics at Surfaces* by A. Zangwill: The first half of this book deals exclusively with clean solid surfaces, with large chunks devoted to metal and semiconductor surfaces. It is positioned at a somewhat similar level to the present article.

- *Theoretical Surface Science; A Microscopic Perspective* by A Gross: The most up to date of the books in this area, with detailed discussions of modern electronic structure theories and their application to metal (and other) surfaces.

- *Concepts in Surface Physics* by M.C. Desjonquères and D. Spanjaard: Provides a very detailed discussion of many aspects of the electronic structures of metals and semiconductors, in particular the basis and application of tight-binding methodologies.

- *Principles of Surface Physics* by F. Bechstedt: Provides a contemporary overview of surface physics from a theoretical microscopic perspective with a particular emphasis on semiconductor surfaces.

- *Handbook of Surface Science, Volume 2* edited by K. Horn and M. Scheffler: Contains several very useful and detailed chapters on the electronic structure of solid surfaces in general (Chapter 1 by E. Wimmer and A. J. Freeman), metal surfaces (Chapter 3 by G. Borstel and J. E. Inglesfield), and semiconductor surfaces (Chapter 2 by J. Pollmann and K. Krüger and Chapter 7 by K. Horn).

- *Interactions of Atoms and Molecules with Solid Surfaces* edited by V. Bortolani, N. H. March, and M. P. Tosi: Although somewhat out of date Chapter 5 by J. E. Inglesfield is excellent, and well worth a read.

- *Theory of the Inhomogeneous Electron Gas* edited by S. Lundqvist and N. H. March: Chapter 5 by N. D. Lang is a good "one stop shop" for most of the early material stemming from the work of Lang and Kohn.

Acknowledgements

AM's work is supported by the European Research Council, the EURYI scheme (see www.esf.org/euryi), and the EPSRC. We are grateful to Bo Li and Ding Pan for helping to prepare some of the figures and to Jiri Klimeš for help in updating parts of sections 3 and 4 prior to publication.

---

[1] D. Shechtman, I. Blech, D. Gratias, and J. W. Cahn, Phys. Rev. Lett. **53**, 1951 (1984).

[2] N. W. Ashcroft and N. D. Mermin, *Solid State Physics* (Saunders College Publishing, Texas, 1985).

[3] F. D. Murnaghan, Proc. Nat. Acad. Sci. U.S.A. **30**, 244 (1944).

[4] It is interesting to note that the definition of a van der Waals bond given by The International Union of Pure and Applied Chemistry (IUPAC) is somewhat different to what we use here. Specifically, van der Waals bonds are defined by IUPAC as *"the attractive or repulsive forces between molecular entities (or between groups within the same molecular entity) other than those due to bond formation or to the electrostatic interaction of ions or of ionic groups with one another or with neutral molecules. This term includes: dipole-dipole, dipole-induced dipole and London (instantaneous induced dipole-induced dipole) forces."* This definition persists largely for historical reasons; originally being used to explain the deviation of gases from ideal-gas behavior.

[5] Www.rsc.org/chemistryworld/podcast/Interactive_Periodic_Table_Transcripts/Krypton.asp.

[6] Helium is left out of this list because its light mass lead it to exhibit special properties due to ensuing strong quantum-mechanical effects/zero-point vibrations.

[7] J. J. Rehr, E. Zaremba, and W. Kohn, Phys. Rev. B **12**, 2062 (1975).

[8] L. Romaner, X. Ren, C. Ambrosch-Draxl, and M. Scheffler, Submitted (2010).

[9] G. A. Jeffrey, *An Introduction to Hydrogen Bonding* (Oxford University Press, New York, 1997).

[10] B. Santra, A. Michaelides, M. Fuchs, A. Tkatchenko, C. Filippi, and M. Scheffler, J. Chem. Phys. **129**, 194111 (2008).

[11] R. M. Dreizler and E. K. U. Gross, *Density Functional Theory* (Springer, Berlin, 1990).

[12] R. G. Parr and W. Yang, *Density Functional Theory of Atoms and Molecules* (Oxford University Press, Oxford, 1994).

[13] In practice, if the system has a net magnetic moment, one may need to perform spin-density functional theory calculations which is a function of 6 variables.

[14] L. H. Thomas, Proc. Cambridge Philos. Soc. **23**, 542 (1927).

[15] E. Fermi, Z. Phys. **48**, 73 (1928).

[16] P. Hohenberg and W. Kohn, Phys. Rev. **136**, 864 (1964).

[17] M. Levy, Proc. Natl. Acad. Sci. **76**, 6062 (1979).

[18] More precisely the second theorem of Hohenberg and Kohn tells us that the ground state electron density can be calculated, in principle exactly, using the variational method involving only the electron density,

$$E_0 = E[n_0] \leq E[n] \quad ,$$

i.e., upon variation, the energy functional, $E[n]$, assumes its minimum value for the ground-state electron density n_0.

[19] W. Kohn and L. Sham, Phys. Rev. **140**, 1133 (1965).

[20] This may also be called "Pauli correlation" because it correlates the dynamics of electrons of like spin. Obviously electrons also repel each other because of their charge.

[21] A distinction between "empirical" and "non-empirical" DFT functionals is also common. Empirical in this context covers those functionals that are designed in order to reproduce experimental results or the results of high-level quantum chemical calculations for quantities such as atomization energies and bond lengths. Typically "training sets" comprised of a large number of well-defined energies and structures of small gas phase molecules are used when making this comparison. The other essentially opposing, non-empirical, strategy is to design functionals that abide by a number of well-known physical constraints which the exact E^{xc} functional should obey and do not include parameters other than fundamental constants.

[22] E. Wigner, Trans. Faraday Soc. **34**, 678 (1938).

[23] M. Gell-man and K. A. Brueckner, Phys. Rev. **106**, 364 (1957).

[24] D. M. Ceperley and B. J. Alder, Phys. Rev. Lett **45**, 566 (1980).

[25] J. P. Perdew and A. Zunger, Phys. Rev. B **23**, 5048 (1981).

[26] J. P. Perdew and J. Yang, Phys. Rev. B **45**, 13244 (1992).

[27] S. J. Vosko, L. Wilk, and M. Nusair, Can. J. Phys. **58**, 1200 (1980).

[28] A note on the nomenclature behind DFT functionals may be appropriate. Functionals are most often named after their authors' in such a way that the name "PBE" comes from a paper by Perdew, Burke, and Ernzerhof. Occasionally the year the paper was published is appended. And if the functional is one of the so-called hydrid functionals, discussed in section 3.2(c) it is common to add the number of parameters used when mixing the Hartree-Fock exchange with the DFT exchange and correlation. For example, PBE0, is a hybrid functional with zero (or at least, at one stage is was argued to have zero) mixing parameters.

[29] O. Gunnarsson and B. I. Lundqvist, Phys. Rev. B **13**, 4274 (1976).

[30] O. Gunnarsson, M. Jonson, and B. I. Lundqvist, Solid State Commun. **24**, 765 (1977).

[31] T. Ziegler, A. Rauk, and E. J. Baerends, Theor Chim. Acta **43**, 261 (1977).

[32] K. Burke, J. P. Perdew, and M. Ernzerhof, J. Chem. Phys. **109**, 3760 (1998).

[33] J. P. Perdew, K. Burke, and M. Ernzerhof, Phys. Rev. Lett. **77**, 3865 (1996).

[34] PBE and its off-spring differ only in how they treat electron exchange. The exchange component of GGA-PBE is

$$E_x^{PBE}[n] = \int n\epsilon^{\text{xc}-\text{unif}}\left(n(\mathbf{r})\right) F_x^{PBE}(n, \nabla n(\mathbf{r}))\, d^3\mathbf{r}$$

where F_x^{PBE} is an exchange enhancement factor given by

$$F_x^{PBE}[n, \nabla n(\mathbf{r})] = 1 + \kappa - \frac{\kappa}{1 + \mu s^2/\kappa}$$

with the dimensionless reduced gradient, $s = |\nabla n|/2n(3\pi^2 n)^{1/3}$. In the original PBE $\kappa = 0.804$. In revPBE $\kappa = 1.245$. In RPBE $F_x[n, \nabla n(r)] = 1+\kappa-\kappa exp(-\mu s^2/\kappa)$, and in PBE-WC μs^2 takes a more complex form.

[35] Y. Zhang and W. Yang, Phys. Rev. Lett. **80**, 890 (1998).

[36] B. Hammer, L. B. Hansen, and J. K. Nørskov, Phys. Rev. B **59**, 7413 (1999).

[37] Z. Wu and R. E. Cohen, Phys. Rev. B **73**, 235116 (2006).

[38] G. K. H. Madsen, Phys. Rev. B **75**, 195108 (2007).

[39] J. P. Perdew, A. Ruzsinszky, G. I. Csonka, O. A. Vydrov, G. E. Scuseria, L. A. Constantin, X. Zhou, and K. Burke, Phys. Rev. Lett. **100**, 136406 (2008).

[40] J. Klimeš, D. R. Bowler, and A. Michaelides, J. Phys.: Cond. Matt. **22**, 022201 (2010).

[41] R. Armiento and A. E. Mattsson, Phys. Rev. B **72**, 085108 (2005).

[42] J. Tao, J. P. Perdew, V. N. Staroverov, and G. E. Scuseria, Phys. Rev. Lett. **91**, 146401 (2003).

[43] J. P. Perdew, A. Ruzsinszky, G. I. Csonka, L. A. Constantin, and J. Sun, Phys. Rev. Lett. **103**, 026403 (2009).

[44] The philosophy behind the hybrid functionals is simple and rooted in the adiabatic connection formula, which is a rigorous *ab initio* formula for the exchange-correlation energy of DFT. One convenient expression of this formula is:

$$E^{xc} = \int_0^1 U_{xc}^{\lambda} d\lambda \quad ,$$

where λ is an interelectronic coupling strength parameter that switches on the $(1/r_{ij})$ Coulomb repulsion between electrons and U_{xc}^{λ} is the potential energy of exchange and correlation at λ. This formula connects the non-interacting reference system with the fully interacting one all at density n. Recognizing that the non-interacting $\lambda = 0$ limit is nothing more than HF exchange, it is expected that exact exchange must play a role in "better" exchange-correlation functionals and thus DFT exchange and correlation functionals are mixed with a fraction of HF exchange.

[45] A. D. Becke, J. Chem. Phys. **98**, 5648 (1993).

[46] C. Adamo and V. Barone, J. Chem. Phys. **110**, 6158 (1999).

[47] J. Heyd, G. Scuseria, and M. Ernzerhof, J. Chem. Phys. **118**, 8207 (2003).

[48] J. Paier, M. Marsman, and G. Kresse, J. Chem. Phys. **127**, 154709 (2007).

[49] S. Kurth, J. P. Perdew, and P. Blaha, Int. J. Quantum Chem. **75**, 889 (1999).

[50] L. M. Almeida, J. P. Perdew, and C. Fiolhais, Phys. Rev. B **66**, 075115 (2002).

[51] C. Fiolhais and L. M. Almeida, Int. J. Quantum Chem. **101**, 645 (2005).

[52] J. P. Perdew, A. Ruzsinszky, J. Tao, V. N. Staroverov, G. E. Scuseria, and G. I. Csonka, J. Chem. Phys. **123**, 062201 (2005).

[53] J. Paier, M. Marsman, K. Hummer, G. Kresse, I. D. Gerber, and J. G. Ángyán, J. Chem. Phys. **124103**, 024 (2006).

[54] J. Harl and G. Kresse, Phys. Rev. Lett. **103**, 056401 (2010).

[55] J. Harl, L. Schimka, and G. Kresse, Phys. Rev. B **81**, 115126 (2010).

[56] L. Schimka, J. Harl, A. Stroppa, A. Grueneis, M. Marsman, F. Mittendorfer, and G. Kresse, Nature Mater. **9**, 741 (2010).

[57] X. Ren and M. Scheffler, Phys. Rev. B **80**, 045402 (2009).

[58] X. Ren, A. Tkatchenko, P. Rinke, and M. Scheffler, Submitted (2010).

[59] E. Wimmer and A. J. Freeman in: *Handbook of Surface Science*, Volume 2; Eds. K. Horn and M. Scheffler (Elsevier, Amsterdam, 2000).

[60] A. E. Mattsson, P. A. Schultz, M. P. Desjarlais, T. R. Mattsson, and K. Leung, Modelling and Simulation in Materials Science and Engineering **13**, 1 (2005).

[61] M. C. Payne, M. P. Teter, D. C. Allan, T. A. Arias, and J. D. Joannopulos, Rev. Mod. Phys. **64**, 1045 (1992).

[62] Sometimes, in particular when atom-centred basis sets are employed, free standing (isolated) slabs are considered. There is, in general, no reason to favor one approach over the other.

[63] M. Fuchs and M. Scheffler, Comput. Phys. Commun. **119**, 67 (1999).

[64] P. E. Blöchl, Phys. Rev. B **50**, 17953 (1994).

[65] M. Bockstedte, A. Kley, J. Neugebauer, and M. Scheffler, Comput. Phys. Commun. **107**, 187 (1997).

[66] D. J. Singh, *Planewaves, Pseudopotentials and the LAPW method* (Kluwer Academic, Boston, 1994).

[67] B. Delley, J. Chem. Phys. **113**, 7756 (2000).

[68] V. Blum, R. Gehrke, F. Hanke, P. Havu, V. Havu, X. Ren, K. Reuter, and M. Scheffler, Comp. Phys. Comm. **180**, 2175 (2009).

[69] D. Pettifor, *Bonding and Structure of Molecules and Solids* (Oxford University Press, Oxford, 1995).

[70] For example the experimental cohesive energies of Li, Na, and K are 1.63, 1.11, and 0.93 eV/atom, respectively [74].

[71] J. P. Perdew, H. Q. Tran, and E. D. Smith, Phys. Rev. B **42**, 11627 (1990).

[72] A. Kiejna, Prog. Surf. Sci. **61**, 85 (1999).

[73] H. T. Tran and J. P. Perdew, Am. J. Phys. **71**, 1048 (2003).

[74] CRC Handbook of Chemistry and Physics, 76^{th} edition, D.R. Lide (Ed.)(CRC Press, Boca

Raton, 1995).

[75] See, for example, C. S. Nichols, *Structure and Bonding in Condensed Matter* (Cambridge University Press, Cambridge, 1995).

[76] M. C. Desjonquères and D. Spanjaard, *Concepts in Surface Physics* (Springer, Berlin, 1998).

[77] The large dip in the PDOS of Mo and other transition metals with half-filled d bands is actually the reason why these elements possess a bcc structure. Systems typically prefer an atomic structure that leads to high electronic "hardness", i.e., low DOS at E_F. Crystallization in an fcc structure, for example, would lead to higher DOS at E_F than is observed for the bcc structure. See ref. [69] for more details.

[78] J. Heyd and G. E. Scuseria, J. Chem. Phys. **121**, 1187 (2004).

[79] J. L. F. DaSilva, C. Stampfl, and M. Scheffler, Surf. Sci. **600**, 703 (2006).

[80] P. Haas, F. Tran, and P. Blaha, Phys. Rev. B **79**, 085104 (2009).

[81] It has been argued that the problem with cohesive energies computed with PBE0 is that the energy of the isolated atoms is badly described [48]. For many other properties, such as adsorption on metals or the size of band gaps in semi-conductors and insulators PBE0 (and hybrid functionals in general) can offer considerably improved performance over LDA, GGAs, and meta-GGAs [48, 206].

[82] T. Todorova, A. P. Seitsonen, J. Hutter, I. F. W. Kuo, and C. J. Mundy, J. Phys. Chem. B **110**, 3685 (2006).

[83] Functionals that include "LYP" correlation [207] must be viewed with some suspicion when dealing with metals since LYP fails to recover the LDA uniform density limit. A consequence, for example, is that the popular B3LYP hybrid functional underestimates the magnitude of the correlation energy in the uniform gas by 30 %. See refs. [49–53], for example, for more discussions on the failings of BLYP and B3LYP for metallic systems.

[84] F. Tran, R. Laskowski, P. Blaha, and K. Schwarz, Phys. Rev. B **75**, 115131 (2007).

[85] A. E. Mattsson, R. Armiento, J. Paier, G. Kresse, J. M. Wills, and T. R. Mattsson, J. Chem. Phys. **128**, 084714 (2008).

[86] G. I. Csonka, J. P. Perdew, A. Ruzsinszky, P. H. T. Philipsen, S. Lebègue, J. Paier, O. A. Vydrov, and J. G. Ángyán, Phys. Rev. B **79**, 155107 (2009).

[87] V. N. Staroverov, G. E. Scuseria, J. Tao, and J. P. Perdew, J. Chem. Phys. **124**, 154709 (2006).

[88] A. A. Stekolnikov, J. Furthmüller, and F. Bechstedt, Phys. Rev. B **65**, 115318 (2002).

[89] M. W. Finnis and V. Heine, J. Phys. F: Metal Phys. **4**, L37 (1974).

[90] R. Smoluchowski, Phys. Rev. **60**, 661 (1941).

[91] U. Landman, R. N. Hill, and M. Mostoller, Phys. Rev. B **21**, 448 (1980).

[92] H. B. Nielsen, J. N. Andersen, L. Petersen, and D. L. Adams, J. Phys. C: Solid State Phys. **15**, 1113 (1982).

[93] G. A. Somorjai, *Introduction to Surface Chemistry and Catalysis* (Wiley, New York, 1994).

[94] R. I. Masel, *Principles of Adsorption and Reaction on Solid Surfaces* (Wiley, New York, 1996).

[95] S. Hengrasmee, K. A. R. Mitchell, P. R. Watson, and S. J. White, Can. J. Phys. **58**, 200 (1980).

[96] G. Michalk, W. Moritz, H. Pfnür, and D. Menzel, Surf. Sci. **129**, 92 (1983).

[97] P. J. Feibelman, Surf. Sci. **360**, 297 (1996).

[98] B. Hamad, Surf. Sci. **602**, 3654 (2008).

[99] B. Santos, J. M. Puerta, J. I. Cerda, T. Herranz, K. F. McCarty, and J. de la Figuera, New J. Phys **12**, 023023 (2010).

[100] S. Titmuss, A. Wander, and D. A. King, Chem. Rev. **96**, 1291 (1996).

[101] M. K. Debe and D. A. King, Phys. Rev. Lett. **39**, 708 (1977).

[102] M. S. Altman, P. J. Estrup, and I. K. Robinson, Phys. Rev. B **38**, 5211 (1988).

[103] H. Landskron, N. Bickel, K. Heinz, G. Schmidtlein, and K. Muller, J. Phys. Condens. Mattter **1**, 1 (1989).

[104] G. Schmidt, H. Zagel, H. Landskron, K. Heinz, K. Muller, and J. B. Pendry, Surf. Sci. **271**, 416 (1992).

[105] C. L. Fu, S. Ohnishi, E. Wimmer, and A. J. Freeman, Phys. Rev. B **53**, 675 (1984).

[106] J. T. Grant, Surf. Sci. **18**, 228 (1969).

[107] N. Bickel and K. Heinz, Surf. Sci. **163**, 435 (1985).

[108] A. Schmidt, W. Meier, L. Hammer, and K. Heinz, J. Phys. Condens. Matt. **14**, 12353 (2002).

[109] S. Hagstrom, H. B. Lyon, and G. A. Somorjai, Phys. Rev. Lett. **15**, 491 (1965).

[110] P. Heilmann, K. Heinz, and K. Müller, Surf. Sci. **83**, 487 (1979).

[111] D. G. Fedak and N. A. Gjostein, Surf. Sci. **8**, 77 (1967).

[112] M. A. VanHove, R. J. Koestner, P. C. Stair, J. P. Biberian, L. L. Kesmodel, I. Bartos, and

G. A. Somorjai, Surf. Sci. **103**, 189 (1981).

[113] M. A. VanHove, R. J. Koestner, P. C. Stair, J. P. Biberian, L. L. Kesmodel, I. Bartos, and G. A. Somorjai, Surf. Sci. **103**, 218 (1981).

[114] P. Havu, V. Blum, V. Havu, P. Rinke, and M. Scheffler, Phys. Rev. B **82**, 161418(R) (2010).

[115] V. Fiorentini, M. Methfessel, and M. Scheffler, Phys. Rev. Lett. **71**, 1051 (1993).

[116] J. Perdereau, J. B. Biberian, and G. E. Rhead, J. Phys. F **4**, 798 (1974).

[117] Y. Tanishiro, H. Kanamori, K. Takayanagi, K. Yagi, and G. Honjo, Surf. Sci. **111**, 395 (1981).

[118] U. Harten, A. M. Lahee, J. P. Toennies, and C. Wöll, Phys. Rev. Lett. **54**, 2619 (1985).

[119] C. Wöll, S. Chiang, R. J. Wilson, and P. H. Lippel, Phys. Rev. B **39**, 7988 (1989).

[120] J. V. Barth, H. Brune, G. Ertl, and R. J. Behm, Phys. Rev. B **42**, 9307 (1990).

[121] W. Moritz and D. Wolf, Surf. Sci. **88**, 29 (1969).

[122] D. L. Adams, H. B. Nielsen, M. A. VanHove, and A. Ignatiev, Surf. Sci. **104**, 47 (1981).

[123] C. M. Chan, M. A. VanHove, W. H. Weinberg, and E. D. Williams, Solid State Commun. **30**, 47 (1979).

[124] E. C. Sowa, M. A. VanHove, and D. L. Adams, Surf. Sci **199**, 174 (1988).

[125] R. Koch, M. Borbonus, O. Hasse, and K. H. Reider, Appl. Phys. A **55**, 417 (1992).

[126] S. J. Jenkins, M. A. Petersen, and D. A. King, Surf. Sci. **494**, 159 (2001).

[127] V. G. Lifshits, A. A. Saranin, and A. V. Zotov, *Surface Phases of Si: Preparation, Structures, and Properties* (Wiley, Chichester, 1994).

[128] G. P. Srivastava, Rep. Prog. Phys. **60**, 561 (1997).

[129] C. B. Duke, Appl. Surf. Sci. **65**, 543 (1993).

[130] C. B. Duke, Chem. Rev. **96**, 1237 (1996).

[131] F. Bechstedt, *Principles of Surface Physics* (Springer, Berlin, 2003).

[132] Duke arrived at five principles. Only the four of relevance to *elemental* semiconductor surfaces are discussed here. The fifth states that "surfaces tend to be autocompensated", which is simply a principle prohibiting the accumulation of charge at the surface. Duke's principles were first reported in ref. [129] and expanded upon in ref. [130]. Subsequent reports of the principles, such an in refs. [128, 131], differ in the number and wording of the principles, although the basic messages which they intend to convey remain unchanged.

[133] A. M. I. Ivanov and J. Pollmann, Surf. Sci. **92**, 365 (1980).

[134] J. Pollmann in: *Handbook of Surface Science*, Volume 2; Eds. K. Horn and M. Scheffler

(Elsevier, Amsterdam, 2000).

[135] P. Krüger and J. Pollmann, Phys. Rev. Lett. **74**, 1155 (1995).

[136] It turns out that dimer reconstructions also explain the c(4×2) and p(2×2) phases of Si(001). These reconstructions with larger unit cells simply originate from different configurations of right- and left-tilted dimers.

[137] J. Dabrowski and M. Scheffler, Appl. Surf. Sci. **56**, 15 (1992).

[138] S. B. Healy, C. Filippi, P. Kratzer, E. Penev, and M. Scheffler, Phys. Rev. Lett. **87**, 016105 (2001).

[139] C. Kress, M. Fiedler, W. G. Schmidt, and F. Bechstedt, Phys. Rev. B **50**, 17697 (1994).

[140] J. Ristein, Appl. Phys. A **82**, 377 (2006).

[141] A. Zangwill, *Physics at Surfaces* (Cambridge University Press, Cambridge, 1988).

[142] J. A. Kubby and J. J. Boland, Surf. Sci. Rep. **26**, 61 (1996).

[143] K. C. Pandey, Phys. Rev. Lett. **47**, 1913 (1981).

[144] K. C. Pandey, Phys. Rev. Lett. **49**, 223 (1982).

[145] X. G. Wang, A. Chaka, and M. Scheffler, Phys. Rev. Lett. **84**, 3650 (2000).

[146] Z. Odziana, N. Y. Tøpsoe, and J. K. Nørskov, Nature Materials **3**, 289 (2004).

[147] G. Wulff, Z. Kristallogr. **34**, 449 (1901).

[148] V. K. Kumikov and K. B. Khokonov, J. Appl. Phys. **54**, 1346 (1983).

[149] It is a simple exercise in elementary thermodynamics to show that G^S and γ are the same for one component systems such as those of interest here. See ref. [93] for example.

[150] W. R. Miller and W. A. Tyson, Surf. Sci. **62**, 267 (1977).

[151] C. Bombis, E. Emundts, M. Nowicki, and H. P. Bonzel, Surf. Sci. **511**, 83 (2002).

[152] D. Yu and M. Scheffler, Phys. Rev. B **70**, 155417 (2004).

[153] It turns out, however, that extreme care must be taken in order to ensure that the surface energy, which is a small energy difference between two much larger total energies is computed reliably. All the issues that can affect the accuracy of the computational set-up, such as basis set, treatment of core electrons, integration over $\boldsymbol{k}$ space, the calculation of the reference bulk atom, the slab thickness, and the slab relaxation must be very carefully checked. See ref. [79] for a more detailed discussion on what is necessary to insure that numerically well-converged values of E^S are computed.

[154] D. C. Langreth and J. P. Perdew, Solid State Comm. **17**, 1425 (1975).

[155] J. P. Perdew, M. Ernzerhof, and K. Burke, J. Chem. Phys. **105**, 9982 (1996).

[156] V. K. Staroverov, G. E. Scuseria, J. Tao, and J. P. Perdew, Phys. Rev. B **69**, 075102 (2004).

[157] R. Armiento and A. E. Mattsson, Phys. Rev. B **72**, 085108 (2005).

[158] S. Overbury, P. Bestrand, and G. A. Somorjai, Chem. Rev. **75**, 547 (1975).

[159] Since E^{coh} is the energy gained upon transformation of a free atom into a bulk atom, unusually high stabilities of atoms with, for example, filled or half filled atomic shells or magnetic ground states can skew the correlation between E^{coh} and E^{S}.

[160] Http://www.webelements.com.

[161] M. Methfessel, D. Hennig, and M. Scheffler, Phys. Rev. B **46**, 4816 (1992).

[162] I. Galanakis, N. Papanikolaou, and P. H. Dederichs, Surf. Sci. **511**, 1 (2002).

[163] D. K. Yu, H. P. Bonzel, and M. Scheffler, Phys. Rev. B **74**, 115408 (2006).

[164] M. Methfessel, D. Hennig, and M. Scheffler, Appl. Phys. A **55**, 442 (1992).

[165] V. Heine, I. J. Robertson, and M. C. Payne, Phil. Trans. Royal Soc. **334**, 393 (1991).

[166] L. Vitos, A. V. Ruban, H. L. Skriver, and J. Kollar, Surf. Sci. **411**, 186 (1998).

[167] I. Galanakis, G. Bihlmayer, V. Bellini, N. Papanikolaou, R. Zeller, S. Blügel, and P. H. Dederichs, Europhys. Lett. **58**, 751 (2002).

[168] J. L. F. DaSilva, C. Barreteau, K. Schroeder, and S. Blügel, Phys. Rev. B **73**, 125402 (2006).

[169] H. P. Bonzel, D. K. Yu, and M. Scheffler, Appl. Phys. A **87**, 391 (2007).

[170] H. P. Bonzel, Physics Reports **385**, 1 (2003).

[171] M. Nowicki, A. Emundts, and H. P. Bonzel, Prog. Surf. Sci. **74**, 123 (2003).

[172] D. K. Yu, H. P. Bonzel, and M. Scheffler, New Journal of Physics **8**, 65 (2006).

[173] N. D. Lang and W. Kohn, Phys. Rev. B **1**, 4555 (1970).

[174] N. D. Lang and W. Kohn, Phys. Rev. B **3**, 12158 (1971).

[175] N. D. Lang, Surf. Sci. **299**, 284 (1994).

[176] N. D. Lang in: *Theory of the Inhomogeneous Electron Gas*; Eds. S. Lundqvist and N. H. March (Plenum Press, New York, 1983).

[177] An alternative and common definition of the work function is that it is the energy difference between a lattice with an equal number of ions and electrons, and the lattice with the same number of ions but with one electron removed [208]. Lang and Kohn explicitly demonstrated that both definitions are equivalent.

[178] Of course, when one looks more closely at the details of the self-consistent electronic struc-

tures obtained from the DFT calculations one finds that the actual details of the electronic redistribution are somewhat more complex than the simple model would suggest. Effects such as *sp* to *d* electron charge transfer and electron flow into the vacuum also play a role, but these will not be discussed here. See ref. [209], for example, for more details.

[179] D. Spanjaard, C. Guillot, M. C. Desjonquères, G. Tréglia, and J. Lecante, Surf. Sci. Rep. **5**, 1 (1985).

[180] J. N. Andersen and C.-O. Almbladh, J. Phys. Condens. Matter **13**, 11267 (2001).

[181] N. Mårtensson, H. B. Saalfeld, H. Kuhlenbeck, and M. Neumann, Phys. Rev. B **39**, 8181 (1989).

[182] J. N. Andersen, D. Hennig, E. Lundgren, M. Methfessel, R. Nyholm, and M. Scheffler, Phys. Rev. B **50**, 17525 (1994).

[183] M. Methfessel, D. Henning, and M. Scheffler, Surf. Sci. **287**, 785 (1993).

[184] M. Aldén, H. L. Skriver, and B. Johansson, Phys. Rev. Let. **71**, 2449 (1993).

[185] M. Methfessel, D. Henning, and M. Scheffler, Surf. Rev. and Let. **2**, 197 (1995).

[186] E. Pehlke and M. Scheffler, Phys. Rev. Lett. **71**, 2338 (1993).

[187] S. G. Davison and M. Stęślicka, *Basic Theory of Surface States* (Oxford University Press, Oxford, 1996).

[188] P. M. Echenique and J. B. Pendry, J. Phys. C **11**, 2065 (1978).

[189] S. Hüfner, *Photoelectron Spectroscopy* (Springer-Verlag, Berlin, 1996).

[190] S. D. Kevan in: *Handbook of Surface Science*, Volume 2; Eds. K. Horn and M. Scheffler (Elsevier, Amsterdam, 2000).

[191] P. Hyldgaard and M. Persson, J. Phys.: Condens. Matter **12**, 2981 (2000).

[192] N. Knorr, H. Brune, M. Epple, A. Hirstein, M. A. Schneider, and K. Kern, Phys. Rev. B **65**, 115420 (2002).

[193] W. Luo and K. A. Fichtorn, Phys. Rev. B **72**, 115433 (2005).

[194] N. F. Crommie, C. P. Lutz, and D. Eigler, Nature **363**, 524 (1993).

[195] Y. Hasegawa and P. Avouris, Phys. Rev. Lett. **71**, 1071 (1993).

[196] W. Shockley, Phys. Rev. **56**, 317 (1939).

[197] I. Tamm, Physik. Zeits. Sowjetunion **1**, 733 (1932).

[198] F. Schiller and C. Laubschat, Phys. Rev. B **74**, 085109 (2006).

[199] P. O. Gartland and B. J. Slagsvold, Phys. Rev. B **12**, 2932 (1975).

[200] S. G. Louie, P. Thiry, R. Pinchaux, Y. Petroff, D. Chandesris, and J. Lecante, Phys. Rev. Lett. **44**, 1782 (1980).

[201] L. Wallden, Solid State Commun. **59**, 205 (1986).

[202] R. Courths, H. Wern, and S. Hufner, Solid State Commun. **61**, 257 (1987).

[203] P. M. Echenique, R. Berndt, E. V. Chulkov, T. Fauster, A. Goldmann, and U. Höfer, Surf. Sci. Rep. **52**, 219 (2004).

[204] E. Bertel, Surf. Sci. **331**, 1136 (1995).

[205] R. Hoffmann, *Solids and Surfaces: A Chemist's View of Bonding in Extended Structures* (VCH, New York, 1988).

[206] K. Doll, Surf. Sci **573**, 464 (2004).

[207] C. Lee, W. Yang, and R. G. Parr, Phys. Rev. B **37**, 385 (1988).

[208] E. Wigner and J. Bardeen, Phys. Rev. **48**, 84 (1935).

[209] M. V. Ganduglia-Pirovano, V. Natoli, M. H. Cohen, J. Kudrnovský, and I. Turek, Phys. Rev. B **54**, 8892 (1996).